Author

John McLain Pray

Title

The morphology of etched and unetched ion tracks in apatite as a function of orientation
and thermal annealing

submitted in partial fulfillment of the requirements for the degree of
Master of Science in Geology
Department of Earth and Environmental Sciences
The University of Michigan

Accepted by:

_R. C. E._	R.C. EWING	8/16/2012
Signature	Name	Date
signature	Maik K. Lang	8/16/2012
Signature	Name	Date
Chris J. Poulsen	Chris J. Poulsen	8/16/2012
Department Chair Signature	Name	Date

I hereby grant the University of Michigan, its heirs and assigns, the non-exclusive right to reproduce and distribute single copies of my thesis, in whole or in part, in any format. I represent and warrant to the University of Michigan that the thesis is an original work, does not infringe or violate any rights of others, and that I make these grants as the sole owner of the rights to my thesis. I understand that I will not receive royalties for any reproduction of this thesis.

☑ Permission granted.

☐ Permission granted to copy after: _____

☐ Permission declined.

J. McLain Pray
Author Signature

Earth and Environmental Sciences
UNIVERSITY OF MICHIGAN

Table of Contents

Abstract

Apatite samples from Durango, Mexico, and Otter Lake, Canada, have been irradiated in different orientations with 185 MeV Xe, 284 MeV Au, and 2.2 GeV Au ions in order to simulate spontaneous fission track formation as a function of annealing temperature, etching time, apatite chemistry, and the orientation of the track relative to the apatite structure. We have characterized the unetched tracks using small angle x-ray scattering and atomic force microscopy and the etched tracks using optical microscopy. Apatite is commonly used in fission track dating, and the data presented here have implications for the use the dating parameter D_{par}, used to assess kinetic annealing rates in apatite. D_{par} is based on the diameter of an "etch figure," or an etched fission track at its intersection with the (10-10) face, measured parallel to the *c*-axis. The D_{par} values are proportional to the annealing rate. Larger D_{par} values indicate slower annealing kinetics. D_{par} measurements of natural apatite have been used to calibrate track-length reduction rates, against which observed track lengths can be evaluated to extract information regarding the thermal history of apatite, such as residence time below 100 °C, as well as the cooling rate.

We observed that etch figures show systematic reductions in diameter with increasing annealing temperature for isochronal heating experiments. This decrease is accompanied by increased variation in diameter, with standard deviations as high as 40% of the mean. This reduction in mean diameter and increase in variability occurs gradually as a function of increasing temperature in the 320-360 °C range, with an accelerated rate in the range 360-400 °C. Extrapolated to geological time and temperature scales, this variation explains the variability reported in the literature for D_{par} measurements on natural apatite, because fission tracks in natural apatite are of different ages and have experienced different amounts of annealing. The decrease in etch figure diameter, however, is proportional to track length decrease during annealing. While the relation between track length and etch figure diameter presented here is simplified, it suggests that the nature of the relation between etch figure diameter and track length is straightforward and that more accurate models of track annealing could be developed. Such models could then be used to correct anomalously low D_{par} values measured in natural apatite by comparison with track length. Also incorporated into this model is the formation of local zones of complete annealing along the track length. These zones have been described as crystalline "gaps" by Green et al. (1986). Since gap formation can occur at random points along the track length, increased variability in track lengths is expected, explaining the increased variation in etch figure diameters at higher annealing temperatures.

The relative sizes of etch figures between Otter Lake and Durango apatite have been compared by calculation of percent differences ($^{\text{difference in diameter}}/_{\text{average of both diameters}}$) for different orientations. A two-fold greater percent difference was observed between (10-11) etch figures than between (10-10) etch figures measured for D_{par} determination. Since kinetic proxy measurements compare relative lengths of etch figures among different apatite grains, the comparison of etch figures on the

(10-11) growth face in addition to the (10-10) growth face may significantly increase the resolution of kinetic proxies used in fission track dating.

Latent (i.e., unetched) tracks were observed using atomic force microscopy (AFM) and small angle X-ray scattering (SAXS). "Hillocks" resulting from irradiation are reported on the surface of unetched apatite. Hillocks have diameters in the range 15-30 nm and heights in the range 3-7 nm, and size dimensions show a systematic dependence on apatite composition and orientation. This dependence is confirmed by SAXS measurements. In addition, etch figure sizes show a similar trend as latent tracks, suggesting that damage production and etching are controlled by similar crystallographic parameters.

Lastly, development of microscopic streaks was observed on surfaces of apatite heated to temperatures above the track-annealing threshold and subsequently etched. These features are approximately 2-20 μm in length, and their origin is unknown.

**Keywords**: apatite, fission track dating, fission track annealing, etch figure, latent tracks

1. Introduction

Apatite – $Ca_5(PO_4)_3(F,Cl,OH)$ – is a common accessory mineral found in a wide variety of geologic environments. Apatite is anisotropic, with hexagonal structure, *P6₃/m*, containing open channels parallel to the *c*-axis (Fig. 1) (Hughes et al., 1990, 1989; Sudarsanan and Young, 1978). The F, Cl and OH occupy this channel. Natural apatite contains uranium in concentrations as high as 200 ppm (Donelick et al., 2005), thus exposing apatite to alpha decay and spontaneous fission events. ^{238}U (the dominant U isotope) undergoes spontaneous fission at a rate of $\sim 10^{-16}$ decays/year, and for every fission event there are approximately 10^6 alpha decays (Fleischer et al., 1975; Steiger and Jäger, 1977; Wagner and Van den haute, 1992). While alpha decay results in an alpha particle and recoil nucleus from the ^{238}U nucleus, fission results in a splitting of the ^{238}U nucleus into two nuclear fragments propelled in opposite directions (Fig. 2). Typical fission fragment masses tend to be bimodal, with the larger and smaller fragments having atomic masses of approximately 135 and 95 amu and energies of approximately 100 and 70 MeV, respectively, for a total energy of ~170 MeV (Fig. 2) (Fleischer, 2004; Möller et al., 2011; Wagner and Van den haute, 1992). This high energy is deposited along the trajectory of the fission fragments, resulting in a cylindrical zone of highly damaged material, fission tracks (FTs), that are approximately 16-20 μm long, with diameters of ~10 nm (Afra et al., 2011; Gleadow et al., 1986; Li et al. 2011; Villa et al., 2000). Once formed, FTs may rapidly recover and begin to anneal due to thermally activated processes (Donelick et al., 1990). Annealing rates depend on temperature, and it is generally accepted that above approximately 100-150 °C, FTs are not preserved over geological timescales (Gleadow and Duddy, 1981; Naeser, 1981; Naeser and Forbes, 1976). Over laboratory timescales, however, FTs can be preserved to much higher temperatures of ~400 °C (Afra et al., 2011; Barbarand et al., 2003b; Carlson et al., 1999; Crowley et al., 1991; Green et al., 1986).
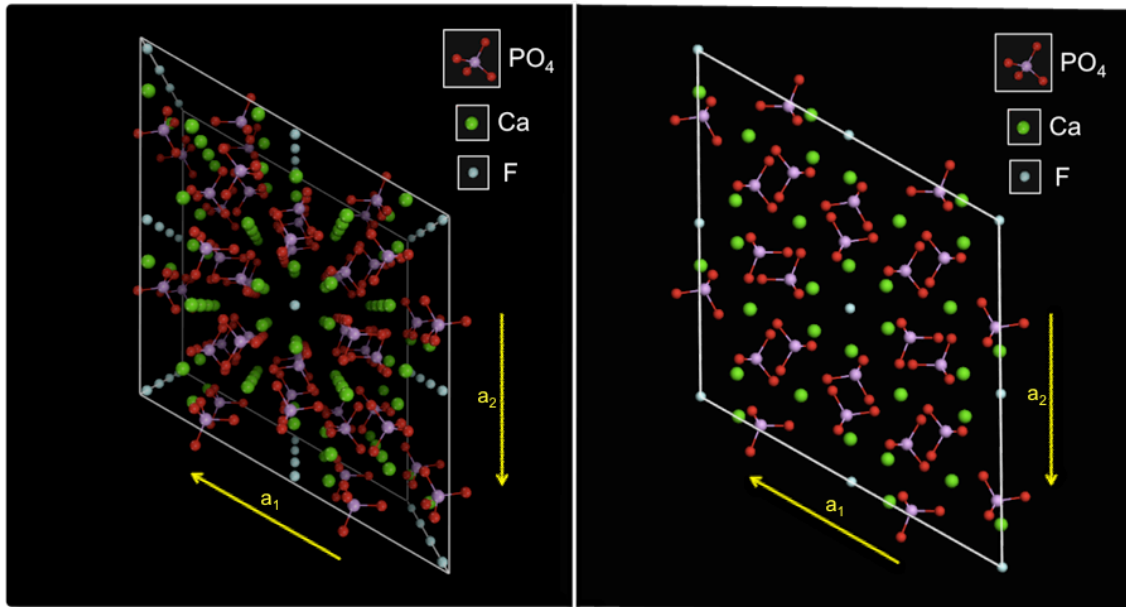
Figure 1: The atomic structure of apatite, shown in perspective view (left) and plan view (right). The a_1- and a_2-axes are labeled. The *c*-axis is normal to the page, such that the *c*-axis is parallel to the hexagonal channels containing the halogen site.
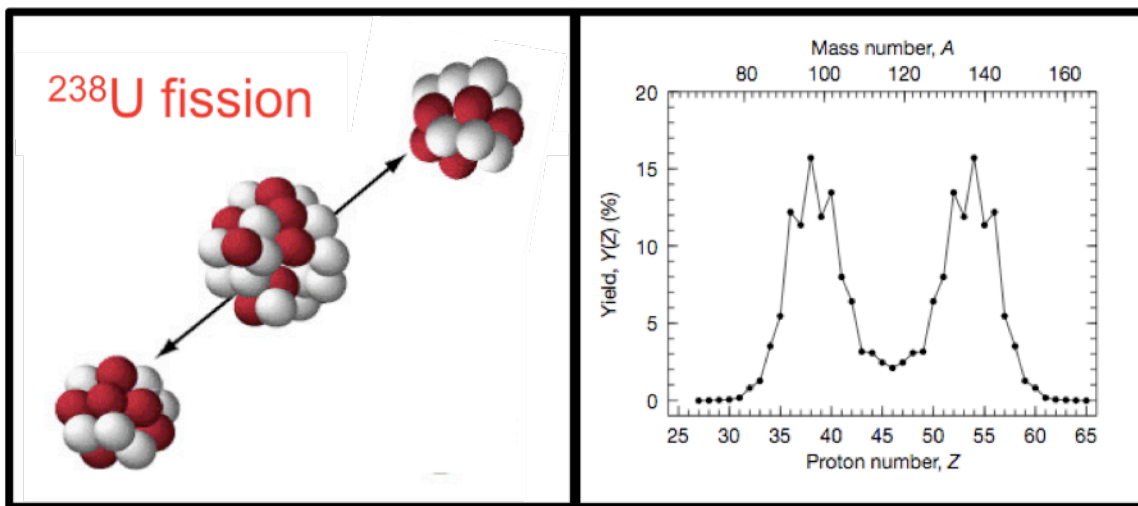
Figure 2: Left: Fission of a ^{238}U nucleus, ejecting daughter products with energies of approximately 100 and 70 MeV, respectively. Figure adapted from Griffith and Rossenfeld (2011). Right: Typical masses of fission products, with average yield percent from electromagnetic-induced fission of ^{234}U, showing bimodal fission product mass distribution. Spontaneous fission of ^{238}U shows analogous behavior, with marginally higher fission product masses. Proton numbers were calculated by assuming Z/N for fission products is the same as for ^{234}U. Figure from Schmidt et al. (2000), adapted by Möller et al. (2001).

The persistence of FTs in apatite below 100-150 °C is the basis FT-dating, an important low-temperature thermochronology technique (Gallagher et al., 1998; Dumitru, 2000; Fleischer et al., 1975; Gleadow et al., 2002; Naeser, 1967; Naeser and McCullough, 1989; Van den haute and de Corte, 1998; Wagner, 1969, 1968; Wagner and Van den haute, 1992). In FT-dating, the number density of FTs in natural

apatite is analyzed in order to determine the regional low-temperature thermal history of Earth's near-surface crust. The present uranium content is compared to FT density in order to constrain the timing of the most recent annealing event, based on the fission track yield and half-life of uranium, given above. In order to see and count FTs, thermochronologists etch the apatite specimens in nitric acid (Fig. 3). Etching increases track diameters from the nm range to the µm range, where they can be observed by an optical microscope. This enlargement occurs because the etchant preferentially attacks the damaged, amorphous material in the track, removing it at a much faster rate than the surrounding undamaged, crystalline matrix. Once amorphous material is removed, etchant diffuses into the track and continues to remove crystalline material from within. Since most natural tracks are completely confined within the crystalline material, etching relies on diffusion of etchant to the track through defects, cleavage planes, or other tracks (Lal et al., 1969). Once etched, FTs can be counted, and the mineral's age below the annealing or "closure" temperature of 100-150 °C – can be determined.
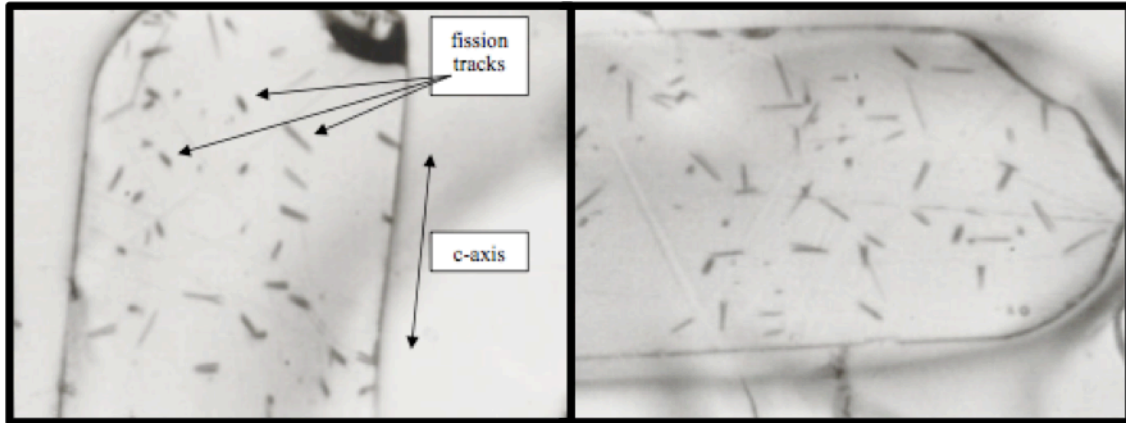

Figure 3: Natural FTs as viewed under optical microscopy after etching in nitric acid. Figure height is approximately 150 µm. Figure from Donelick et al. (2005).

In addition to track density, track length distribution is used to infer more detailed information about the cooling rate (Bhandari et al., 1971; Crowley, 1985; Donelick and Miller, 1991; Gleadow et al., 1986, 1983; Ketcham, 2003; Laslett et al., 1982; Wagner and Storzer, 1972). Laboratory and bore-hole studies have demonstrated that FT annealing is characterized by track shortening (Gleadow and Duddy, 1981; Naeser, 1981; Naeser and Forbes, 1976). These studies have shown that the track annealing rate is strongly temperature dependent, showing a non-linear length decrease with annealing temperature, as shown by Figure 4. For FT-dating, models have been developed to quantify track shortening over geological timescales as a function of time and temperature (Gleadow and Duddy, 1981; Ketcham et al., 1999; Vrolijk et al., 1992). A wide distribution of track lengths is taken to indicate a slow, gradual cooling rate, exposing tracks to relatively high temperatures for relatively long time intervals, such that appreciable track-shortening occurs. In this case, track lengths are inversely proportional to track age. On the other hand, a narrow distribution of long FTs represents a rapid cooling rate, followed by a long residence time at cooler temperatures, such that significant

thermal annealing does not occur. In this case, older tracks are not significantly shorter than younger tracks. Alternatively, a low track density indicates a rapid cooling rate followed by a short residence time at cool temperatures, such that tracks did not have ample time to accumulate.

In order to quantify track lengths accurately, thermochronologists have developed standard etching procedures intended to etch tracks fully, without "over-etching," i.e. removing an appreciable amount of crystalline material from the ends of the track (Carlson et al., 1999; Donelick et al., 2005; Ketcham et al., 1999; Ravenhurst et. al, 2003; Sobel and Seward, 2010). In so doing, only tracks that have been etched by etchant diffusion through another track are considered (Carlson et al., 1999, Donelick et al., 2005, 1990; Jonckheere and Wagner, 2000). This is because tracks intersecting defects may have larger-than-normal lengths, since fission products travelling through a defect have greater range than fission products that travel only through crystalline material; tracks intersecting cleavage planes, on the other hand, have lower-than-expected annealing rates (Barbarand et al., 2003a).
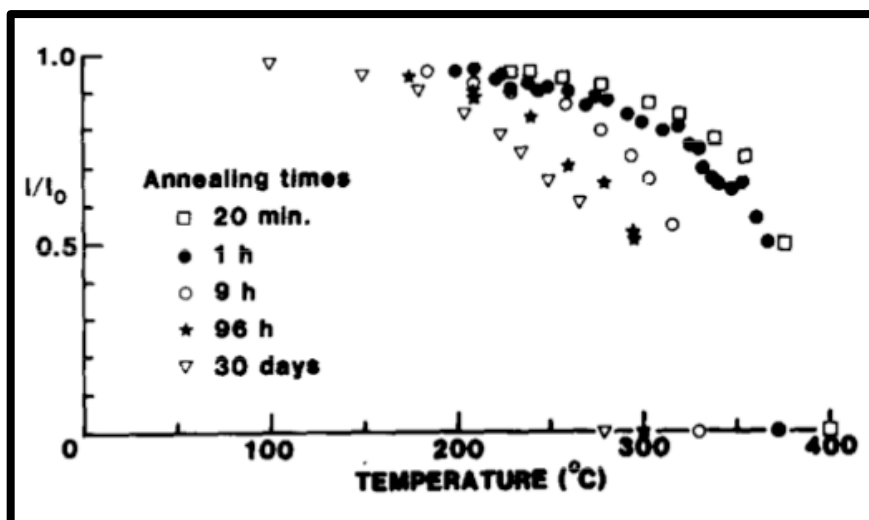
Figure 4: Track shortening shown as a function of annealing time and temperature. The vertical axis, labeled "l/l_0," represents measured track length divided by unannealed track length. The figure shows an accelerated length reduction with increasing temperature. Figure from Green et al. (1986).

However, it has been demonstrated that FTs in apatite show different annealing rates – and therefore different track shortening rates – depending mostly on variations in chemistry (Burtner et al., 1994; Carlson et al., 1999; Crowley et al., 1991; Gleadow and Duddy, 1981; Green et al., 1986, 1985; O'Sullivan and Parrish, 1995), but also on crystallographic orientation of the FT (Donelick, 1991; Donelick et al., 1999; Donelick and Miller, 1991; Ketcham, 2003; Vrolijk et al., 1992), the extent of alpha decay damage (Hendriks and Redfield, 2005), and possibly the confining pressure (Lang et al., 2008; Wendt et al., 2002). The most important control over annealing kinetics is Cl-content, and it is generally accepted that higher Cl-content correlates with slower annealing rates (Barbarand et al., 2003b; Carlson et al., 1999; Crowley et al., 1991; Green et al., 1985). However, chemical analysis of Cl-content on individual grains is not commonly done in most FT-dating studies.

Instead, an alternate proxy for annealing kinetics has been developed. This proxy, called "D_{par}," is defined as the diameter of an etched FT where it intersects the apatite surface along a polished (10-10) plane (the prismatic growth face), measured parallel to the *c*-axis (Fig. 5) (Burtner et al., 1994; Donelick, 1993; Stockli et al., 2001). The morphology of the etched fission track at the surface of a specimen, as viewed under optical microscopy, is called an "etch figure." Since etch figures elongate parallel to the *c*-axis during etching, the orientation of D_{par} measurements is easily identified. D_{par} values correlate inversely with annealing rates, i.e. larger track diameters correlate with slower annealing kinetics (Barbarand et al., 2003b; Burtner et al., 1994; Carlson et al., 1999; Donelick, 1993; Sobel and Seward, 2010). In addition, D_{par} has been shown to vary proportionately with Cl-content (Donelick, 1993; Donelick et al., 2005). D_{par} measurement is easily integrated into the FT-dating procedure. Because apatite grains are prepared for track-length analysis by polishing the (10-10) plane followed by etching, D_{par} measurements can be made simultaneously with track length measurements (Donelick, 1993).
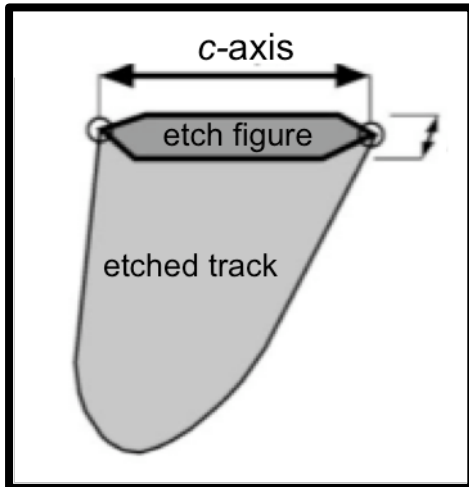

Figure 5: A schematic of etch figure morphology as seen on the apatite (10-10) plane. Etch figure elongation is in the direction of the crystallographic *c*-axis. Average etch figure diameter, D_{par}, on the (10-10) plane is used as kinetic proxy in the FT-dating method. Figure adapted from Sobel and Seward (2010).

Much understanding of annealing behavior has been gained by studying the morphology of etched FTs, but progress is still limited, as etching destroys the latent track morphology, such that fundamental characteristics of FTs cannot be observed (Crowley et al., 1991). However, recent studies using small angle X-ray scattering (SAXS) and transmission electron microscopy (TEM) have brought new insights into the atomic-scale structure of FTs and their annealing characteristics. SAXS is a non-destructive technique that allows size determination of nm-size objects in solids, based on scattering of X-rays due to electron density fluctuations (~1% sensitivity) over nm-length scales. Due to their large aspect ratios, latent tracks are very good scattering centers and thus can be examined under SAXS. Previous SAXS studies on artificial ion tracks (ITs) produced at an ion accelerator have shown that tracks consist of a combination of extended and point defects, and that latent, unannealed ion tracks in apatite have diameters of approximately 10 nm, with diameter decreasing during (Fig. 6) (Afra et al., 2011; Durrani and Bull, 1987). This decrease parallels track length decrease during annealing as observed using etched tracks, as discussed above (Fig. 4). Studying ITs with TEM, Li et al. (2012) showed that track

shortening is actually due to this diameter decrease. Since tracks have a conical morphology, diameter decrease along the track length results in track shortening (Fig. 7). Carlson (1990) had previously suggested this behavior in natural FTs and developed models for track shortening based on conical track morphology (Fig. 8).
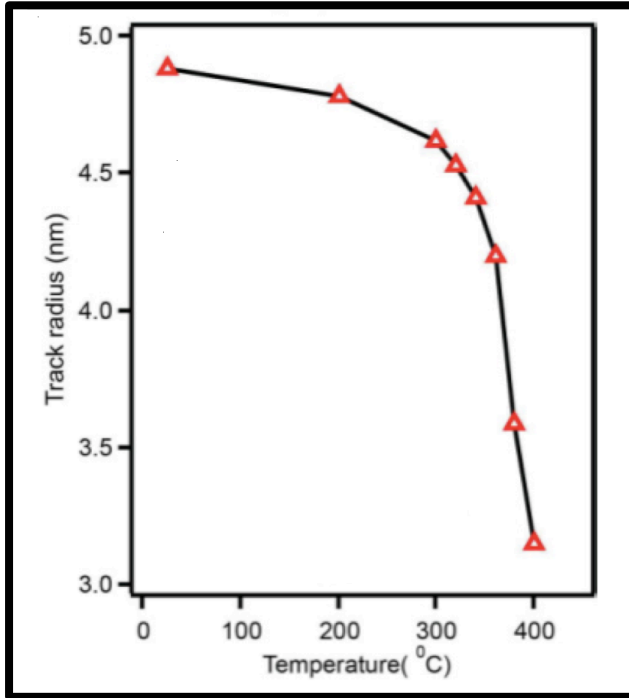
Figure 6: SAXS data showing systematic decrease in track diameter with increasing annealing temperature, for constant annealing times (30 min.). Figure adapted from Afra et al. (2011).
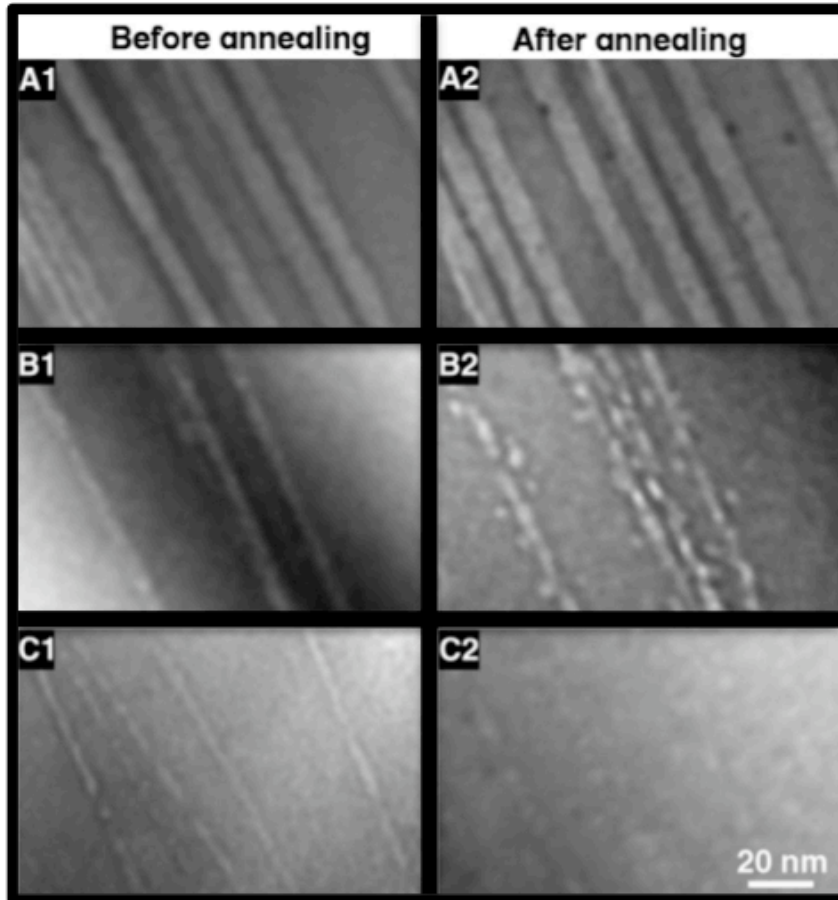
Figure 7: *In situ* TEM images of annealing behavior of ITs in apatite, showing preferential annealing at the inner tip of the track, relative to the top of the track near the mineral surface, due to lower initial diameter and faster diameter reduction at the track tip. The latent track lengths were approximately 8-9 μm. The boxes marked (A) show tracks in the near surface region; the boxes marked (B) show the middle of the track at depths of 4.5 μm; the boxes marked (C) show the inner tip of the track, at depths of 7.2 μm. No diameter reduction was seen in the near-surface after heating at 330 °C for 1 h and additional heating at 380 °C for 1 h. In contrast, significant diameter reduction was accompanied by crystalline gap formation at depths of 4.5 μm when exposed to the same heating conditions. However, almost complete annealing was observed at 7.2 μm depth after heating at 330 °C for only 16 min. Figure from Li et al. (2012).
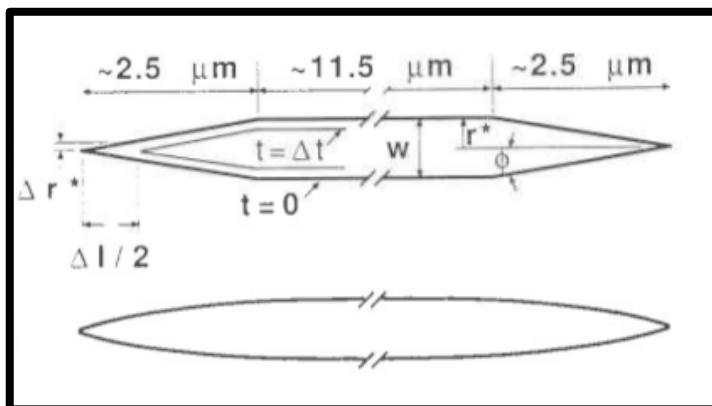
Figure 8: Bottom: FT morphology proposed by Carlson (1990), showing gradual diameter taper with distance from the center of the track. Top: A simplified morphology used by Carlson (1990) in mathematical models to simulate track shortening with annealing time. Figure from Carlson (1990).

Green et al. (1986) suggested that tracks may segment because of the formation of gaps filled with crystalline material during the later stages of annealing, due to complete recrystallization at random points along the track length (Fig. 9). This suggestion was based on the observation of partially annealed tracks that appeared to be fully etched after 20 s, but then suddenly increased in length after 30 s (Fig. 10). This delayed renewal of etching was attributed to the presence of a crystalline gap that had developed during annealing. Only after the gap had been breached by the etchant could the remaining track length be etched. Carlson (1990) suggested that latent tracks show only slight taper within the central 11.5 μm of track length (Fig. 8). Thus, after track shortening to 11.5 μm, local oscillations in latent track diameter may cause the formation of crystalline gaps at any point along the track length. The experimental results of Green et al. (1986) agree with this model, except suggesting that gap formation begins when tracks reach lengths of 8 μm, not 11.5 μm. Crystalline gap formation was verified at the atomic scale by Li et al. (2012), as shown in Figure 7, Box B2. These observations confirm that gap formation occurs just prior to the onset of complete annealing.
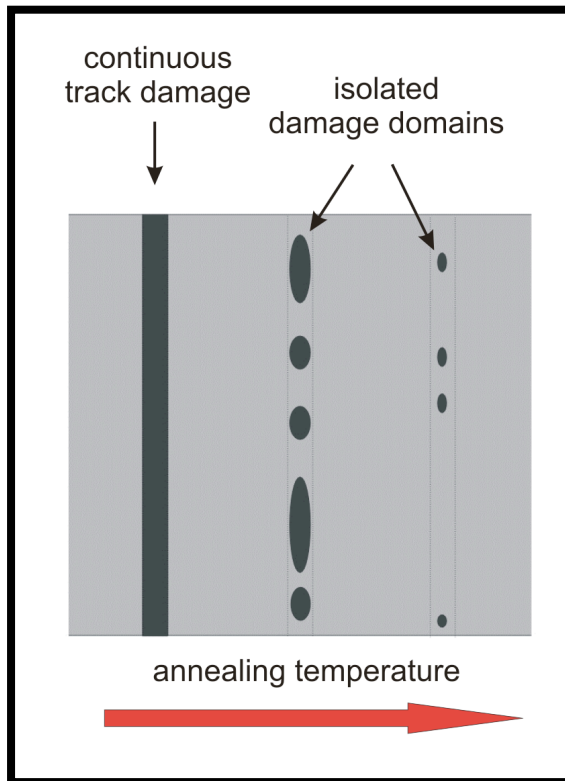
Figure 9: A schematic showing the development of crystalline gaps during annealing, leading to the segmentation of amorphous material as hypothesized by Green et al. (1986). The track to the left is unannealed; the track in the center is partially annealed, with several crystalline gaps isolating amorphous zones; the track to the right shows nearly complete annealing, such that only small amorphous domains remain. Figure from Lang (2001).
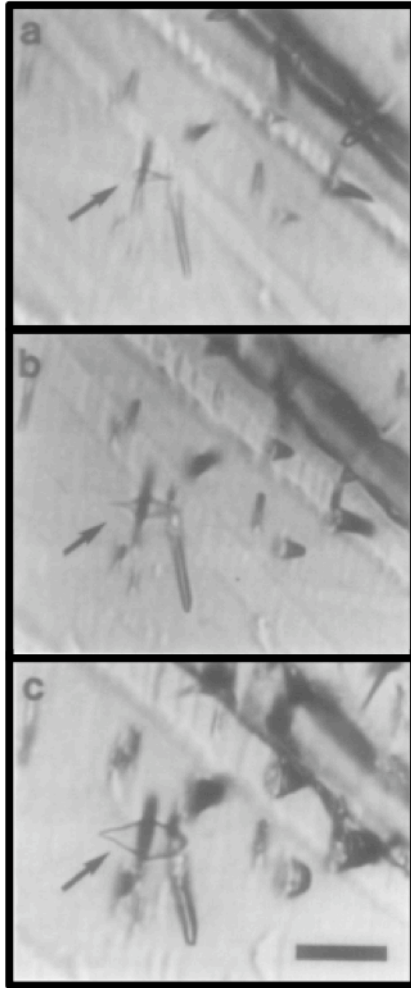
**Figure 10:** Sequential photomicrographs taken of the same confined FT (shown by arrow) in a Durango apatite specimen annealed at 352 °C for 1 h and etched with 5 M nitric acid. Image (a) was taken after 20 s of etching and shows etching on the right side of the track. Image (b) was taken after 30 s of etching and shows sudden commencement of etching on the left side of the track, indicating that a crystalline gap had delayed etching on the left side. Image (c) was taken after 50 s of etching, showing full etching on both sides of the track. The bar in the lower right corner of image (c) is 10 μm in length. Figure from Green et al. (1986).

In this study, both unetched and etched track diameters have been investigated for two apatite samples of different composition, as a function of annealing temperature, etching time, and crystallographic orientation. Hitherto, no systematic study has been performed on the effects of annealing on etch figure diameter. Rather, it has been assumed that etch figure diameter does not vary as a function of annealing. This assumption is the basis for the D_{par} parameter, since any proxy for annealing rates must not vary with the extent of annealing. FTs were simulated by ion irradiation using Xe accelerated to 185 MeV and Au accelerated to 284 MeV and 2.2 GeV. Although natural fission fragments have lower energies, Villa et al. (1999) showed that it is not the total energy deposition that is important for determination of track diameter, but rather the energy loss rate, $^{dE}/_{dx}$, of the projectile as it decelerates in a material. Figure 11 shows the energy loss rates in fluorapatite for ions and energies used in this study, as compared to fission product energies. As can be seen, energy loss rates are similar, suggesting that ITs used in this study are good simulations of FTs. Track lengths are also comparable. While etched natural FTs are approximately 16 μm in length, calculations using the software program "Stopping and Range of Ions in Matter" (SRIM) indicate approximate ion ranges of 14.8 and 18.5 μm for 185 MeV Xe and 284 MeV Au,

respectively (Ziegler et al., 2010). By using artificial ITs instead of natural FTs, track orientation and the density of tracks in the apatite can be controlled exactly. This important improvement in experimental technique provides the basis for our systematic investigation of etch figure diameters.
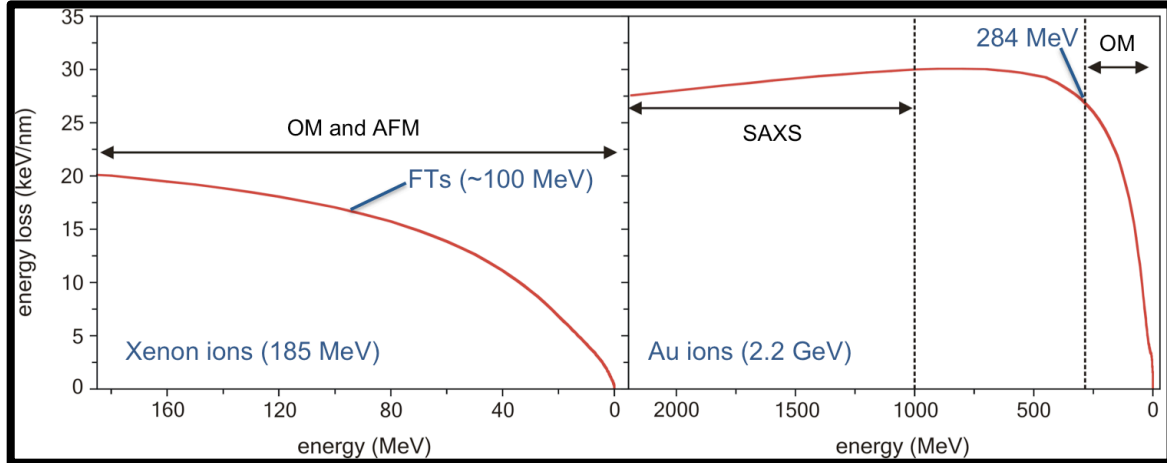

Figure 11: A summary of the energy loss rates ($\frac{dE}{dx}$) for 185 MeV Xe, 100 MeV Xe, 2.2 GeV Au, and 284 MeV Au projectiles as a function of depth in fluoroapatite, as determined by SRIM code (Ziegler et al., 2010). Arrows indicate the energy ranges of ions used in this study. For the same ion type, lower energy ions can be plotted on the same curve as higher energy ions because ion velocity and energy loss depend only on the current energy of the ion. Thus a 2.2 GeV Au ion that has been reduced to 284 MeV has the same velocity and energy loss rate as an Au ion that started with 284 MeV energy. The left shows the complete energy loss of 185 MeV Xe ions, which were used for optical microscopy (OM) and AFM. The right shows two energy regimes. The higher was used for SAXS and indicates that projectiles passed completely through the material with a near constant energy loss rate, resulting in tracks with uniform diameter. The lower was used for OM and indicates that ions stopped within the material. 100 MeV Xe is marked on the graph to the left representing typical energy loss rates of fission daughter products. Note however, that track formation is accomplished by two daughter products, so the energy loss profile shown in the figure only represents half of a FT.

This study used three analytical techniques: optical microscopy, SAXS, and atomic force microscopy (AFM). Etch figures were measured as a function of annealing temperature and etching time using optical microscopy. Latent tracks were characterized by SAXS and AFM. While SAXS detects latent track diameters averaged over the entire track length, AFM detects individual surface features on the nm-scale. Thus AFM was used to analyze the surface morphology of irradiated surfaces. Previous studies have reported the formation of hillocks on the surface of irradiated materials, due to expansion of material upon irradiation, according to the thermal-spike model (Fleischer et al., 1967; Lang et al., 2002; Müller et al., 2002; Zhang et al., 2009). However, hillock formation has never been reported in apatite. By investigating both etched and unetched tracks, the relation between latent and etched track morphology could be investigated.

16

2. Experimental Methods

Two natural apatite samples were used in this study: Durango, from Durango, Mexico, and Otter Lake, from Quebec, Canada. Both varieties are reported in the literature as near end-member fluorapatite, with Durango having a Cl-content of approximately 0.12 anions per formula unit, and Otter Lake having negligible amounts of Cl (Barbarand et al., 2003b; Carlson et al., 1999; Ravenhurst et al., 2003; Young et al., 1969). Samples of both Durango and Otter Lake apatite were cut and polished along four crystallographic orientations: the (10-10) prismatic growth face, the (10-11) pyramidal growth face, the (0001) basal plane, and the (2-1-10) face, which is perpendicular to the (10-10) face and parallel to the c-axis (Fig. 12).
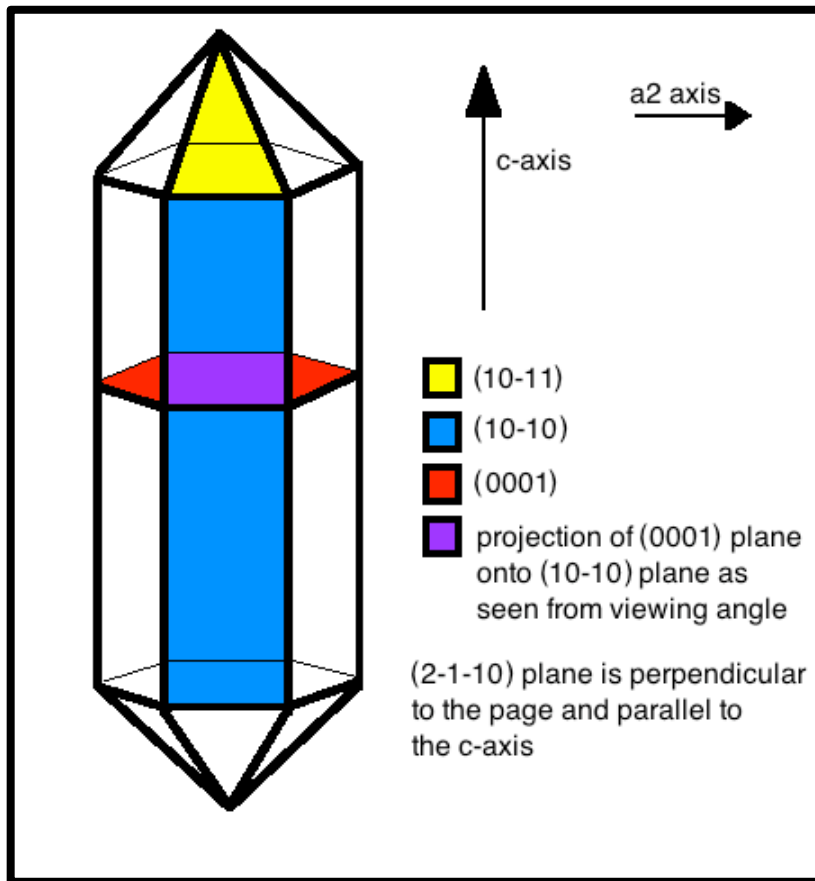
Figure 12: Schematic of an apatite crystal, showing the hexagonal symmetry and highlighting the crystallographic orientations used in this study. (10-10) is the prismatic plane, (0001) is the basal plane, (10-11) is the pyramidal plane, and (2-1-10) is the vertical plane projected out of the page. The (10-10) and (0001) faces intersect in projection to the viewing angle, and the intersection has been colored purple.

Sample chemistry was determined using a CAMECA SX-100 Electron Microprobe Analyzer, controlled by CAMECA PeakSight software using the X-Phi matrix correction program (Merlet, 1994) at the University of Michigan Electron Microbeam Analysis Laboratory. Both (10-10) and (0001) oriented samples of unannealed Durango and Otter Lake apatite were analyzed. Samples were mounted

in epoxy resin and polished to approximately 1 mm thickness using diamond and aluminum lapping paper. A carbon coat of approximately 200-Å thickness was applied to the sample surfaces by thermal evaporation, as determined by the method of Kerrick et al. (1973). Samples were mounted flat so the electron beam bombardment was normal to the polished surface. Standards included synthetic end-member chlorapatite for Ca and P, natural fluortopaz for F, synthetic Ba-Cl apatite for Cl, natural celestite for S, and natural almandine garnet for Si. Standard compositions are shown in Table 1. Beam size was 10 μm, with column conditions of 15 keV and 10 nA. The low beam current and voltage, as well as the large beam spot size, were set to specifications reported in the literature used to minimize diffusion of F and Cl under the electron beam (Henderson, 2011; Stormer et al., 1993). Data collection times were: 10 s for Ca, 20 s for P, Si, and S, and 30 s for Cl and F. O concentration was determined by oxide calculation.

Table 1: Minerals used as elemental standards for electron microprobe analysis, with chemical composition in elemental weight percent.

Element	Mineral Standard	Standard Composition (wt%)
F	Fluortopaz	Al: 29.3206% Si: 15.2601% O: 34.774% F: 20.6454%
Ca, P	Chlorapatite	Ca: 38.4812% P: 17.8429% O: 36.8681% Cl: 6.8078%
Cl	Ba-Cl apatite	P: 9.23% O: 19.06% Cl: 3.52% Ba: 68.18%
Si	Almandine	Ca: 1.24% Al: 11.91% Si: 17.95% O: 41.94% Na: 0.09% Mg: 5.03% Ti: 0.03% Cr: 0.03% Mn: 1.69% Fe: 20.61%
S	Celestite	Sr: 47.7026% S: 17.4543% O: 34.8431%

Samples were prepared for irradiation by polishing to thicknesses of approximately 100-200 μm for optical microscopy and AFM and approximately 40 ± 10 μm for SAXS. Samples were polished to a roughness of approximately 10 nm, using diamond and aluminum lapping paper. Since the Durango and Otter Lake samples are natural specimens, each was annealed at 450°C for 24 hours to remove all accumulated natural radiation damage. Samples were irradiated normal to the polished surface with 185 MeV Xe, 284 MeV Au, or 2.2 GeV Au ions at GSI Helmholtzzentrum für Schwerionenforschung, in Darmstadt, Germany. Irradiation fluences were adjusted to appropriate levels for each analysis technique: 5×10^4, 1×10^{10}, and 5×10^{10} ions/cm^2 for optical microscopy, AFM, and SAXS, respectively. Higher fluences were used for SAXS because SAXS data is statistical, representing the average size of millions of tracks (Durrani and Bull, 1987).

For optical microscopy, 185 MeV Xe- and 284 MeV Au-irradiated specimens were annealed for 30 minutes at a constant temperature between 320-420 °C in a Thermo Scientific FB1315M furnace, while other specimens were left unannealed. Furnace temperatures were verified by two independent thermocouples, and temperatures agreed within ± 5 °C. For annealing, specimens from each apatite composition (Durango and Otter Lake) and each orientation were annealed simultaneously in the same oven. After annealing, all samples annealed at the same temperature were etched together on the same glass holder by oscillating the holder back and forth smoothly in a beaker of 0.55 M nitric acid at room temperature (21 °C). The nitric acid etching solution was prepared by dilution of laboratory-standard 16 M nitric acid. After etching, samples were immediately rinsed in running deionized water. The 0.55 M etchant was used rather than stronger etchants often used in FT-dating in order to allow longer etching times and thereby eliminate the significance of timing errors between samples on different slides.

After etching, samples were viewed under reflected light using a Nikon Optiphot optical microscope with 1000x magnification, using a 100x dry objective lens and 10x ocular lenses, with a GIF filter to increase contrast. Etch figure diameters were measured along the largest cross section, as is standard practice in making D_{par} measurements. Average etch figure diameters and standard deviations were determined in general from 50 etch pits; however, for a limited number of samples, fewer etch pits were used. Etch figure diameters and morphology were then compared as a function of apatite composition, crystallographic orientation, annealing temperature, and the duration of etching. In total, approximately 3000 measurements were made.

SAXS was performed on unannealed, unetched, 2.2 GeV Au-irradiated specimens at the SAXS/WAXS beamline at the Australian Synchrotron. The higher energies for SAXS measurements were used in order to induce tracks that penetrated completely through the polished samples. This ensured an almost constant energy loss ($^{dE}/_{dx}$) over the entire sample thickness, resulting in uniform track diameters through the specimen. Experimental details are identical to those used in Afra et al. (2011) and can be found therein. In addition to irradiated specimens, unirradiated specimens were analyzed as well, and resulting patterns were used as the basis for background subtraction. SAXS measurements were repeated several times, and we verified that track diameters were constant as a

function of time during the synchrotron analysis; thus the use of synchrotron source X-rays can be considered to be nondestructive.

AFM was performed in contact mode in air on unannealed, 185 MeV Au-irradiated specimens, using a Veeco Enviroscope controlled by Nanoscope Version 5.30r3.sr3 software. Aluminum-coated, silicon Vista probes were used, with 0.1 N/m spring constant and nominal tip radius of < 10 nm. Scan size was 1 μm, and scan rate was 2 Hz.

3. Results

3.1 Electron Microprobe Analysis: apatite compositions

Results from electron microprobe analysis (EPMA) are shown in Table 2. Measurements showed higher F- and Cl-content during analysis normal to the (0001) orientation than for the (10-10) orientation, in agreement with the observations of Stormer et al. (1993). As explained in Stormer et al. (1993), this diffusion is likely due to the channeled structure of apatite in the *c*-axis direction (Fig. 1). In the Otter Lake specimens, F- and Cl-content were 6-7% higher for the (0001) orientation than for the (10-10) orientation, while Durango specimens showed 10% higher F-content for the (0001) orientation, but only 0.4% higher Cl-content. Thus, only the data from the (10-10) orientation should be considered quantitatively accurate, but the relative trend for both orientations shows that Otter Lake apatite is more F-rich than Durango, and Durango is more Cl-rich, although both apatite have low Cl/F ratios. The Cl-content for Otter Lake was negligibly small, as detected concentrations were below detection limits. The Cl-content of Durango – approximately 0.77 formula units – is lower than the 0.12 formula units reported in the literature by Carlson et al. (1999). This is likely because natural specimens inherently show chemical variations.

The F-content in Otter Lake apatite was greater than one formula unit, indicating an anomalous result. However, similar results were reported by Ravenhurst et al. (2003), without explanation. The total weight percentages (wt%) were lower for Otter Lake apatite than Durango apatite, indicating a possible source of error for Otter Lake measurements due to incomplete detection of elemental concentrations. Ravenhurst et al. (2003) reported CO_2 levels of 0.82 wt% in Otter Lake apatite. Assuming this CO_2 concentration in the specimen used here, wt% sums are nearly 99%. Since OH-content could not be determined in EPMA analysis, literature values of 0.08 wt% OH were assumed (Ravenhurst et al., 2003). With these assumed OH and CO_2 concentrations, average formula units were calculated and are displayed in the bottom row of Table 2. In addition to the differing F- and Cl-content mentioned above, the Otter Lake specimen showed an appreciable Si-content (0.473 wt%), while the Durango specimen did not.

Table 2: EPMA data determined for Otter Lake and Durango apatite. Since (0001) orientations produce inaccurate results (Stormer et al., 1993), only the (10-10) data should be taken as representative of the apatite used in this study. Final calculations of average formula units for each element using the (10-10) data, with assumed CO_2 and OH concentrations from Ravenhurst et al. (2003), are shown in red.

Sample/Point	Weight% F	Cl	P	Ca	Si	S	O	Total
D (10-10) 1	3.5793	0.5251	17.6100	38.3215	0.1113	0.1952	38.3613	98.7035
D (10-10) 2	3.5176	0.5344	17.7722	38.6607	0.1103	0.1837	38.6937	99.4727
D (10-10) 3	3.6165	0.4948	17.7653	38.4056	0.1095	0.1930	38.5912	99.1759
D (10-10) 4	3.5460	0.5442	17.6597	38.2319	0.1123	0.1738	38.3696	98.6376
D (10-10) 5	3.5457	0.5023	17.9287	38.1906	0.1099	0.1890	38.7129	99.1791
OL (10-10) 1	4.5790	0.0353	16.7749	38.3286	0.4736	0.1898	37.6931	98.0741
OL (10-10) 2	4.3449	0.0419	16.7347	38.4805	0.4595	0.2057	37.7017	97.9689
OL (10-10) 3	4.3412	0.0320	16.6952	38.0855	0.4422	0.1863	37.4539	97.2363
OL (10-10) 4	4.4691	0.0347	16.7592	38.2658	0.4782	0.2193	37.6825	97.9087
OL (10-10) 5	4.3742	0.0236	16.6330	38.6612	0.4524	0.1906	37.6192	97.9541
OL (10-10) 6	4.3875	0.0220	16.8788	38.5421	0.4630	0.2267	37.9374	98.4575
OL (10-10) 7	4.3525	0.0223	16.7527	38.5544	0.4730	0.2274	37.7914	98.1736
OL (10-10) 8	4.3516	0.0421	16.7819	38.3112	0.4915	0.2034	37.7291	97.9108
OL (10-10) 9	4.3482	0.0293	16.7861	38.0202	0.4940	0.2638	37.6815	97.6231
OL (10-10) 10	4.3469	0.0318	16.5567	38.4268	0.5026	0.2251	37.5188	97.6087
D (0001) 1	3.9250	0.5239	17.8515	38.9003	0.1187	0.1630	38.8805	100.3629
D (0001) 2	3.9861	0.5280	17.8467	38.7256	0.1100	0.1439	38.7755	100.1158
D (0001) 3	3.9110	0.5222	17.9775	38.0698	0.1087	0.1883	38.7255	99.5028
D (0001) 4	3.8770	0.5234	18.1044	38.4148	0.1021	0.2034	39.0348	100.2600
D (0001) 5	3.9134	0.5143	17.8543	38.3015	0.1031	0.1596	38.6238	99.4699
OL (0001) 1	4.5783	0.0248	16.7615	38.5929	0.4727	0.1738	37.7644	98.3684
OL (0001) 2	5.2979	0.0333	16.5008	38.3301	0.4812	0.1895	37.3482	98.1812
OL (0001) 3	4.5821	0.0442	16.5037	38.3106	0.4815	0.2169	37.3716	97.5105
OL (0001) 4	4.4752	0.0316	16.5934	38.3159	0.4624	0.1825	37.4337	97.4947
OL (0001) 5	4.5013	0.0334	16.8044	38.2241	0.4900	0.1730	37.6914	97.9176

Sample	Average Weight%							
	F	Cl	P	Ca	Si	S	O	Total
D (10-10)	3.5610	0.5202	17.7472	38.3621	0.1107	0.1869	38.5457	99.0338
OL (10-10)	4.3895	0.0315	16.7353	38.3676	0.4730	0.2138	37.6809	97.8916
D (0001)	3.9225	0.5224	17.9269	38.4824	0.1085	0.1716	38.8080	99.9423
OL (0001)	4.6870	0.0335	16.6328	38.3547	0.4776	0.1871	37.5219	97.8945

	Average Weight% including CO_2 and OH* *CO_2 and OH content from Ravenhurst et al. (2003)									
	F	Cl	P	Ca	Si	S	O	C	H	Total
D (10-10)	3.5610	0.5202	17.7472	38.3621	0.1107	0.1869	38.5007	0.0082	0.0047	99.0017
OL (10-10)	4.3895	0.0315	16.7353	38.3676	0.4730	0.2138	38.3523	0.2238	0.0047	98.7916
D (0001)	3.9225	0.5224	17.9269	38.4824	0.1085	0.1716	38.9051	0.0082	0.0047	100.0523
OL (0001)	4.6870	0.0335	16.6328	38.3547	0.4776	0.1871	38.1933	0.2238	0.0047	98.7945

|	Average Formula Units									
	F	Cl	P	Ca	Si	S	O	C	H	
D (10-10)	0.9792	0.0766	2.9934	5.0006	0.0206	0.0305	12.5711	0.0036	0.0246	
OL (10-10)	1.2069	0.0046	2.8223	5.0006	0.0880	0.0348	12.5210	0.0973	0.0246	
D (0001)	1.0750	0.0767	3.0134	4.9992	0.0201	0.0279	12.6599	0.0035	0.0246	
OL (0001)	1.2888	0.0049	2.8053	4.9995	0.0888	0.0305	12.4703	0.0973	0.0246	

3.2 Optical Microscopy: etched tracks

Photomicrographs of typical irradiated specimens after etching are shown in plan view in Figure 13. Etch figures are consistent in size and morphology, with the expected hexagonal morphology and elongation in the direction of the c-axis for the c-axis-parallel (10-10) and (2-1-10) orientations. The etch figure aspect ratios along the (10-10) plane are lower than is commonly observed with tracks etched with 5.5 M acid, as is common for FT-dating (Fig. 14). This is due to the lower concentration of the etchant (0.55 M), as reported in Ravenhurst et al. (2003). Since the c-axis does not lie in the (10-11) plane, (10-11) etch figures are not elongated in the direction of the c-axis, but rather in the direction of the c-axis projection onto the (10-11) plane. The (0001) etch figures are expected to be perfectly hexagonal, i.e. showing no elongation, since they are perpendicular to the c-axis. However, Otter Lake (0001) etch figures show an asymmetric elongation, having only one mirror plane. Grivet et al. (1993) report similar etch figures in Durango apatite cut along the (10-10) plane, without explanation (Fig. 15). This asymmetry has not been reported by other authors, suggesting that the crystal alignment used in Grivet et al. (1993) may have been in error, and that misalignment may produce asymmetric etch figures. However, Grivet et al. (1993) used 1% (~0.16 M) HNO_3 etchant, which is nearly 3.5 times weaker than the 0.55 M etchant used in this study. Thus, as with etch figures with low aspect ratios, asymmetric etch figures may be associated with low etchant concentrations.
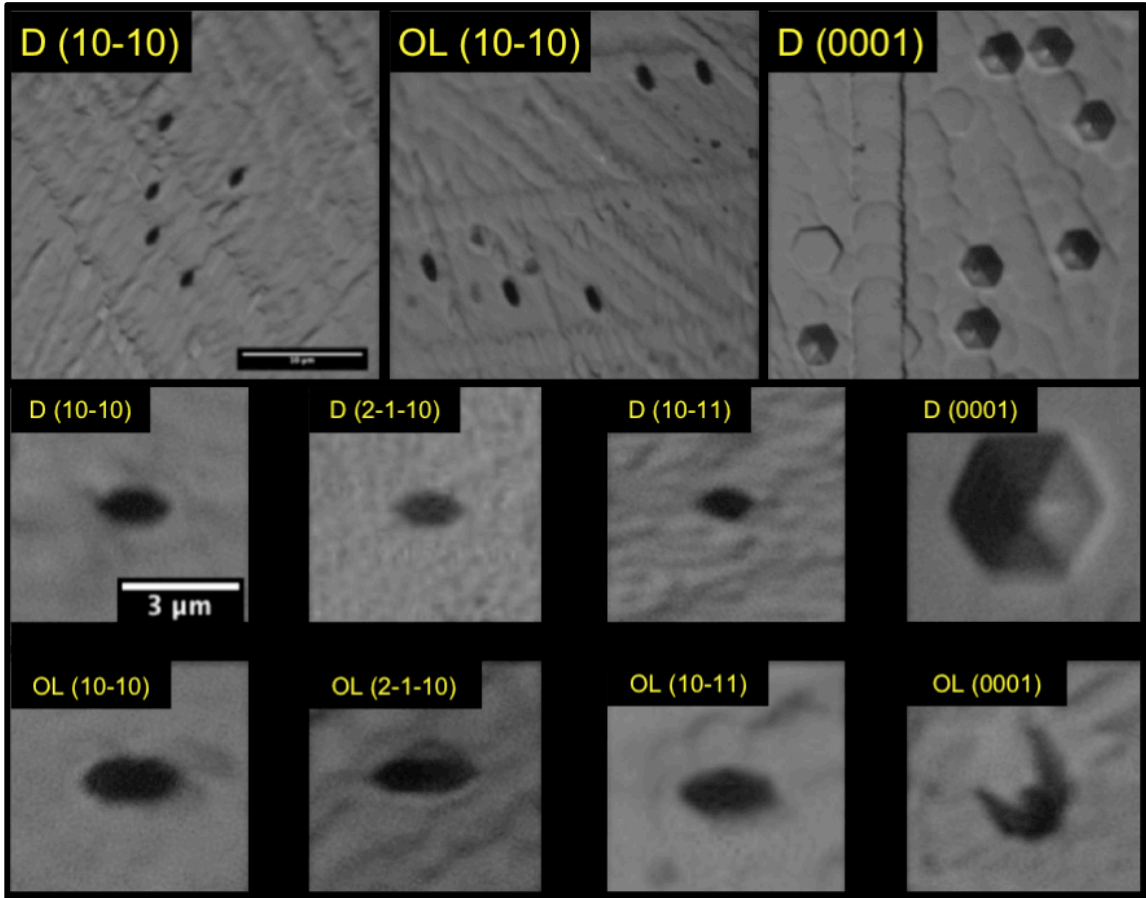
Figure 13: Above: Typical photomicrographs of specimens after etching for 90 s. Etch figures are parallel with uniform size and morphology. Below: Photomicrographs showing the relative sizes and morphology of etch figures from each sample after 90 s of etching.
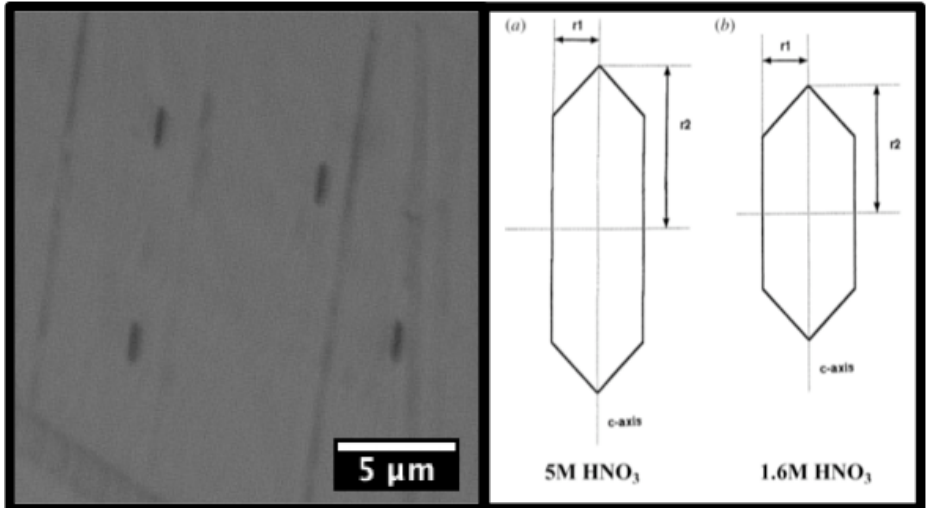
Figure 14: Left: Durango (10-10) etch figures after etching for 20 s in 5.5 M nitric acid, showing much higher aspect ratios than Durango (10-10) etch figures shown in Figure 13. Right: A schematic of (10-10) etch figures observed on apatite as a function of etchant concentration, showing decreased aspect ratio with decreased etchant concentration. Units are arbitrary since etch figure morphology is not observed to change as a function of etching time for a single etchant concentration. Image to the right from Ravenhurst et al. (2003).
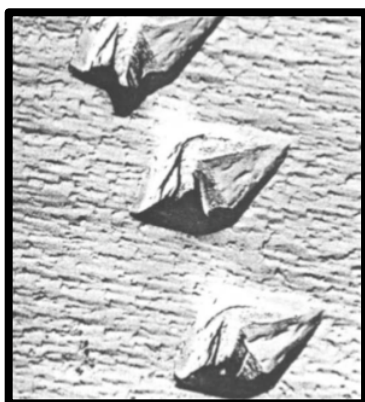
Figure 15: TEM images of Durango (10-10) etch figures reported in Grivet et al. (1993), showing asymmetric etch figures. The images were produced using a platinum shadowed carbon replica method. Scale: 0.5 cm = 1 μm. Figure from Grivet et al. (1993).

Etch figure diameters were determined by measuring etch figures on photomicrographs along the maximum diameter from left to right, as oriented in the bottom two rows in Figure 13. Otter Lake (0001) etch figures were not measured along the longest dimension because the endpoints along the top corner of these etch figures often could not be resolved by optical microscopy, due to the shallow gradient of the etch pit. Rather, Otter Lake (0001) etch figures were measured along the largest diameter perpendicular to the overall largest diameter.

As a function of etching time, etch figure diameters were observed to increase linearly, in agreement with many other etch-track studies (e.g., Ravenhurst et al., 2003; Sobel and Seward, 2010), at rates of approximately 0.01-0.03 $\mu m/s$. Figure 16 shows the increase in etch figure diameter as a function of etching time for the Otter Lake (0001) orientation. Because unetched tracks are only approximately 10 nm wide (Li et al., 2011), the line of best fit was set to intercept the origin. There is no point at 30 s because etch figures were too small to be measured. In addition to the linear increase in etch figure diameter, etch figure morphology was not observed to change as a function of etching time, showing identical aspect ratios for all etch steps.
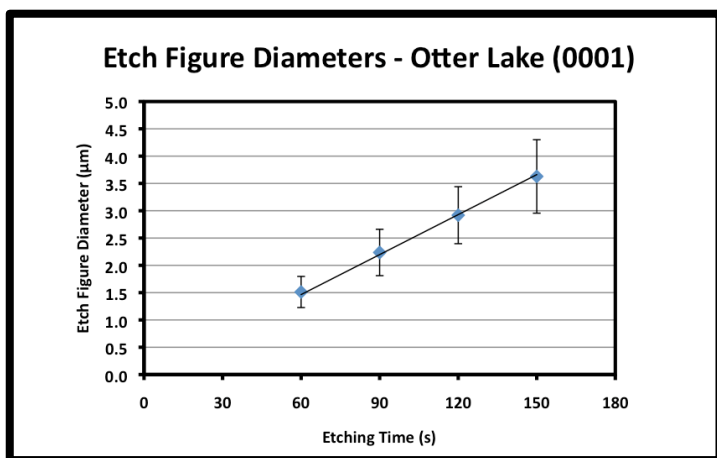
Figure 16: Etch figure diameter increase as a function of etching time, showing a linear relation. Linear relations were observed for all samples. Error bars are for two-sigma.

As a function of orientation, etch figure diameters are largest for the (0001) orientation and smallest for the (10-11) orientation. The Durango (10-10) and (2-1-10) etch figures show nearly identical morphology, although the (10-10) etch figures are both slightly longer and wider. Otter Lake (10-10) and (2-1-10) orientations show greater differences in morphology, with the former being shorter and wider. As noted above, (0001) morphology is considerably different between Durango and Otter Lake samples.

Comparing etch figure diameters as a function of apatite composition, Otter Lake etch figures have greater diameters than Durango etch figures for all but the (0001) orientation. However, since Otter Lake and Durango (0001) samples show considerably different morphology, and since diameter measurement orientation for Otter Lake (0001) tracks was not along the longest diameter, the (0001) etch figure diameters cannot be compared quantitatively. Differences in average etch figure diameters between Durango and Otter Lake apatite for the (10-10), (2-1-10), and (10-11) orientations are summarized in Table 3. For each orientation, difference was calculated as a percentage by the following formula:

$$\% \text{ Difference} = \frac{^{(\text{OL etch figure diameter – D etch figure diameter})}}{_{\text{Average of both diameters}}} *100$$

As can be seen from Table 3, (10-11) etch figures show the greatest diameter difference, followed by the (2-1-10) orientation, with the (10-10) orientation showing the least difference.

Orientation	% Difference
(10-10)	29
(2-1-10)	37
(10-11)	56

Table 3: Percent differences in average etch figure diameter observed between Durango and Otter Lake apatite, as a function of orientation and temperature.

Table 4 and Figure 17 show mean etch figure diameters with errors after 90 s etching time for samples irradiated with 284 MeV Au, as a function of composition, orientation, and annealing temperature. Some samples were lost during the experiment and are marked "N/A" in Table 4. These data points are omitted from Figure 17.

Table 4: Etch figure diameters, standard deviations, and standard error (error of the mean) for Au-irradiated specimens, reported as a function of temperature, apatite composition, and orientation.

Sample	Annealing Temperature (°C)	Diameter (μm)	Standard Deviation (μm)	Standard Error (μm)
Durango (10-10)	unannealed	1.75	0.11	0.02
	320	1.73	0.14	0.02
	340	1.74	0.12	0.02
	360	1.67	0.28	0.04
	380	no tracks*		
	400	no tracks*		
	420	no tracks		
Otter Lake (10-10)	unannealed	2.29	0.17	0.02
	320	N/A		
	340	2.28	0.23	0.03
	360	2.30	0.31	0.04
	380	no tracks*		
	400	no tracks		
	420	no tracks		
Durango (2-1-10)	unannealed	N/A		
	320	1.64	0.16	0.02
	340	N/A		
	360	N/A		
	380	1.31	0.29	0.04
	400	no tracks*		
	420	no tracks		
Otter Lake (2-1-10)	unannealed	2.43	0.15	0.02
	320	2.40	0.18	0.03
	340◆	1.97	0.05	0.01
	360	1.93	0.34	0.05
	380	no tracks		
	400	no tracks		
	420	no tracks		
Durango (10-11)	unannealed	1.15	0.08	0.01
	320	1.10	0.08	0.01
	340	1.19	0.12	0.02
	360	1.17	0.13	0.02
	380	no tracks		
	400	no tracks		
	420	no tracks		

Otter Lake (10-11)	unannealed	2.13	0.13	0.02
	320	2.10	0.16	0.02
	340	1.94	0.35	0.05
	360	1.98	0.30	0.04
	380	no tracks		
	400	no tracks		
	420	no tracks		
Durango (0001)	unannealed	3.14	0.32	0.05
	320	N/A		
	340	N/A		
	360	N/A		
	380	2.79	0.41	0.06
	400	2.45	0.98	0.14
	420	no tracks		
Otter Lake (0001)	unannealed	2.24	0.23	0.03
	320	2.25	0.23	0.03
	340	2.14	0.24	0.03
	360	1.88	0.40	0.06
	380	2.21+	0.38	0.09
	400	no tracks		
	420	no tracks		

*anomalous streaks observed
♦based on only 4 measurements
+based on only 17 measurements
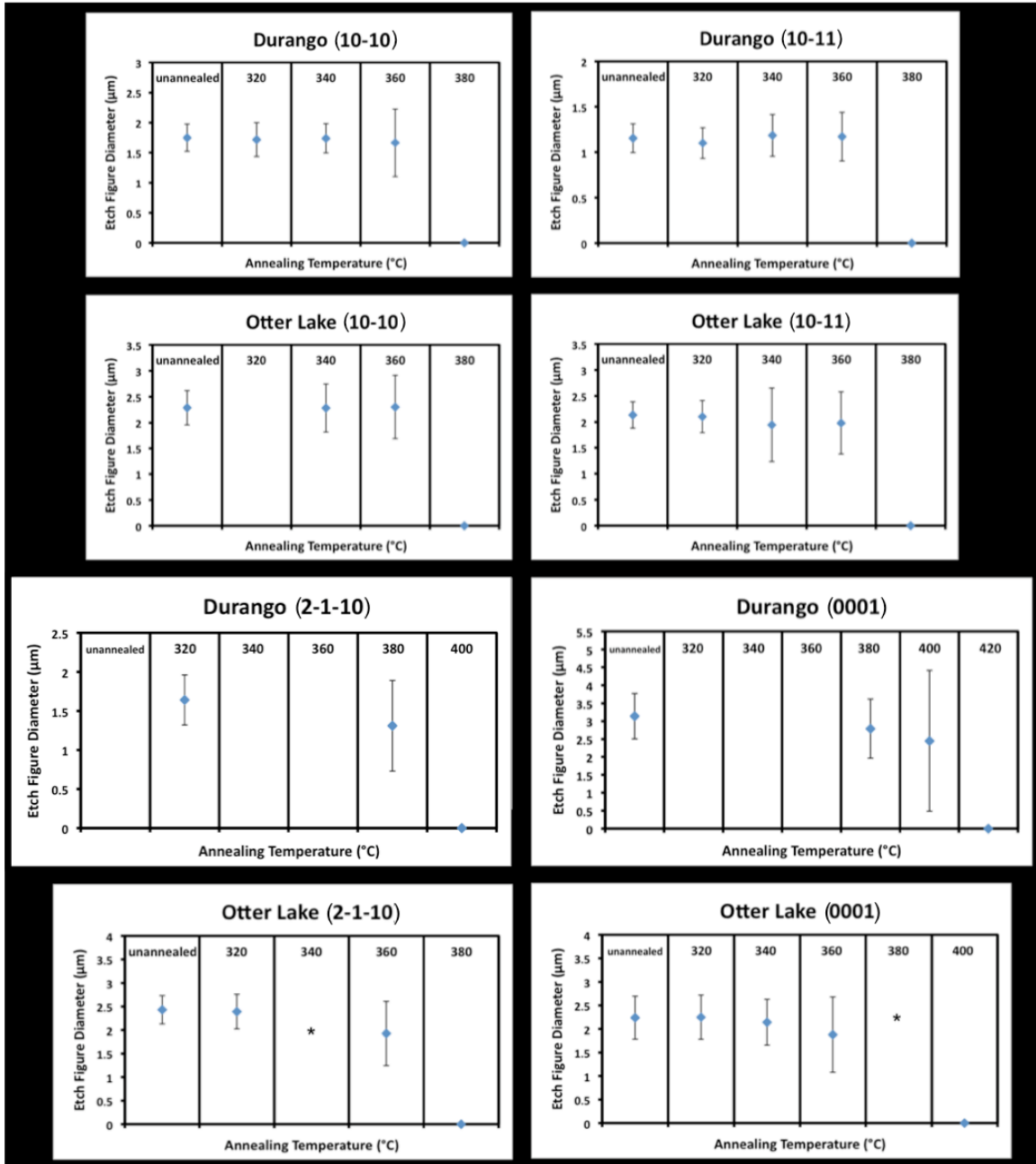
Figure 17: Average etch figure diameters after 90 s etching for different apatite samples and orientations, before and after annealing at different temperatures. Error bars are for two-sigma. A * indicates a potentially erroneous measurement based on a limited sample size – see discussion in text and footnote to Table 4.

As a function of increasing temperature, a general trend of decreasing etch figure diameter was observed. The rate of etch figure reduction with increased temperature was not uniform across all samples. Rather, some samples showed a strong decrease, while others showed little to no decrease. In general, however, etch figure decrease accelerated with temperature, showing very gradual decreases for low temperatures, and then sudden decreases above a certain temperature threshold, followed by erasure of tracks usually at the next-higher temperature,

indicating track annealing. As used here, track annealing implies that tracks are no longer etchable. Although atomic-scale techniques such as TEM and SAXS may still be able to detect the presence of segmented amorphous material, as discussed in the Introduction, for the purposes of this discussion, specimens which lack etch figures are considered to be annealed.

The Otter Lake (10-10) and Durango (10-11) samples showed no decrease in etch figure diameter with temperature, followed by sudden erasure of tracks, indicating annealing. While this observation is certainly accurate for the Otter Lake (10-10) samples, the lack of measureable variation for the Durango (10-11) may also be attributed to the small sizes of these etch figures. Since the average etch figure diameter of Durango (10-11) – 1.1-1.2 μm – is only slightly greater than resolution of an optical microscope (~0.7 μm, the highest wavelengths on the visible light spectrum), variation in etch figure diameter is very difficult to detect.

On the other hand, the largest etch figures – along the (0001) orientation – showed clear decrease in average diameter with temperature. The 380 °C and 400 °C Durango (0001) specimens showed 13% and 28% lower average etch figure diameters than the unannealed Durango (0001) specimen. The 360 °C Otter Lake (0001) specimen showed a 19% lower average etch figure diameter than the unannealed Otter Lake (0001) specimen. The subsequent increase in diameter at 380 °C is anomalous, but only 17 etch figures were observed on this specimen, suggesting the sample size may not be statistically significant. In addition, these tracks showed very obscure morphology (Fig. 18), and the specimen surface showed a dimpled texture, implying partial recrystallization of surface features such as polishing scratches during annealing. This recrystallization may have caused surface features, track regions, and polishing scratches to become blurred, such that the resulting etch figures are more representative of surface topology than track morphology. Due to this interaction, smaller etch figures may have been obscured, rendering an anomalously high average etch figure diameter. Thus, the average etch figure diameter observed on Otter Lake (0001) at 380 °C may be anomalous. The corresponding data point is therefore suspect and is marked with an asterisk in Figure 17.
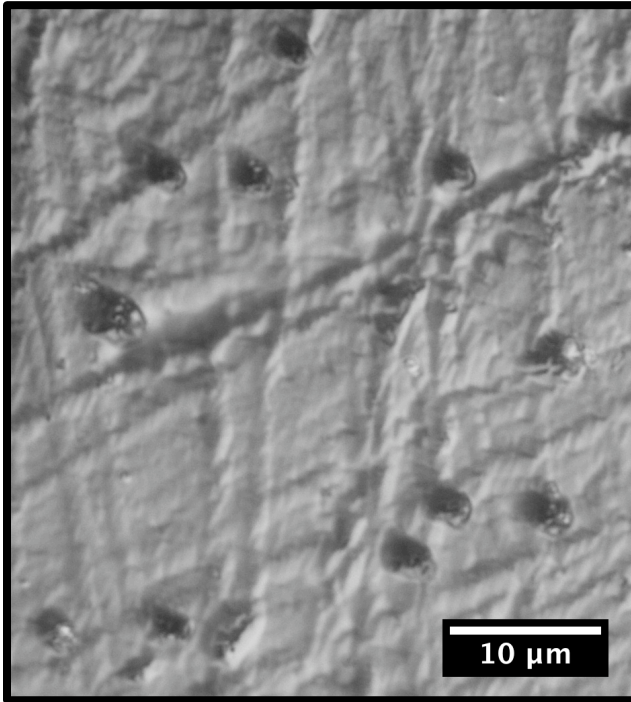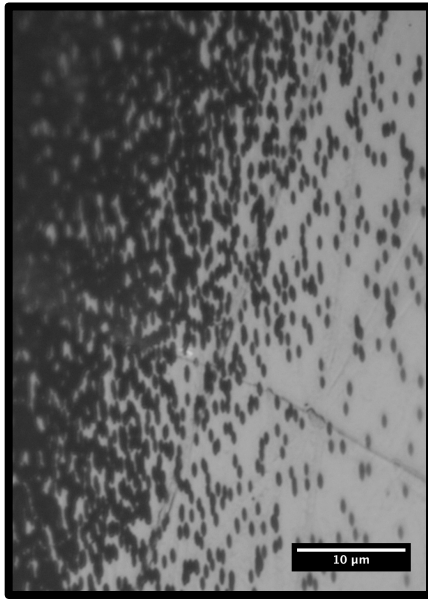
Figure 18: Otter Lake (0001) specimen annealed at 380 °C, showing diffuse etch figure morphology, and dimpled sample surface indicating partial recrystallization of polishing scratches during annealing.

Displayed in Table 5 are the results from samples irradiated with 185 MeV Xe. For this set of samples, the actual track density was higher than anticipated due to beam calibration problems. This resulted in multiply-overlapping etch figures, such that individual etch figures in general could not be identified (Fig. 19, on left). However, the Otter Lake (10-10) specimen was on the edge of the irradiation sample holder and received lower ion fluences on their outer edges, resulting in low-enough track density that individual etch figures could be measured for two specimens, those annealed at 340 and 380 °C (Fig. 19). Both specimens showed diameters comparable to Otter Lake (10-10) specimens irradiated with Au ions. Note however, that no tracks were observed at 380 °C for samples irradiated with Au, suggesting that the Xe tracks were preserved to higher temperatures than the Au tracks. Although diameters could not be measured, annealing temperatures could be determined for Xe-irradiated specimens simply by observing whether or not tracks were present. While annealing temperatures were the same as Au tracks for the Durango (10-10) and (2-1-10) apatite, the Otter Lake (10-10), Durango (10-11), Otter Lake (0001), and Durango (2-1-10) apatite showed annealing temperatures 20 °C higher for Xe tracks than for Au tracks. On the other hand, one Xe-irradiated specimen – Durango (0001) – showed annealing at 20 °C lower than the Au-irradiated Durango (0001) samples.

A second observation of etching behavior as a function of annealing was a larger distribution of etch figure diameters with increasing temperature, as expressed by greater standard deviations as shown in Tables 4 and 5, and Figures 17. Representative photomicrographs of specimens showing large diameter distributions are shown in Figure 20. For all specimens, standard deviation increased at least two-fold between unannealed specimens and the highest temperature specimens on which etch figures were observed. In two cases –

Durango (0001) irradiated with Au and Otter Lake (10-10) irradiated with Xe – this difference was three-fold. Like the accelerated decrease in etch figure diameter, standard deviation showed accelerated increase at temperatures approaching the annealing threshold. The only sample that did not show a sudden increase in standard deviation near the annealing threshold was Durango (10-11). However, as remarked above, the small size of these etch figures indicates that differences in diameter are difficult to measure, and the variability in measured diameters is more likely the result of measurement errors than true diameter differences.

Figure 19: Otter Lake (10-10) specimen annealed at 340 ℃, after 60 s of etching, showing very high irradiation fluence to the left, with decreasing track density to the right, such that etch figure diameters could be measured.
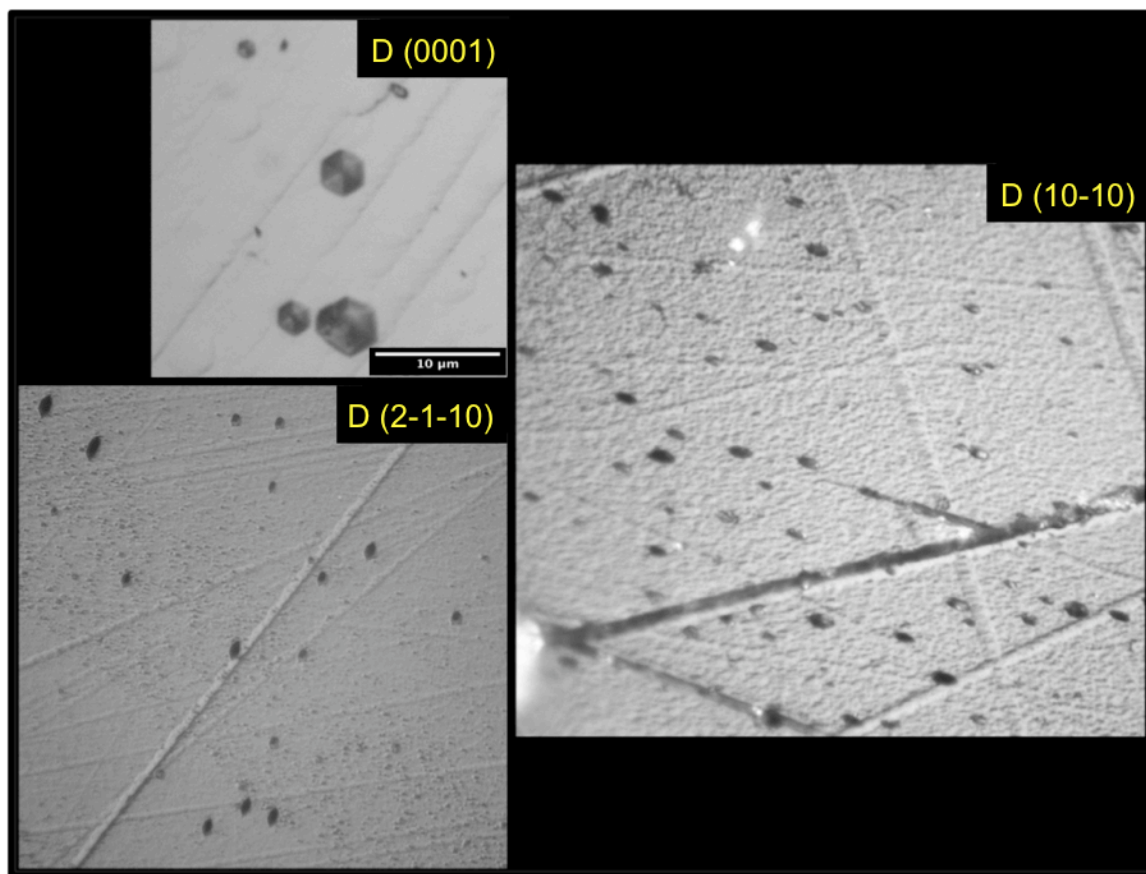
Figure 20: Representative photomicrographs of samples showing enhanced variation in etch figure diameter at high temperatures. Upper Left: Au-irradiated Durango (0001) annealed at 400 °C; this specimen showed the greatest standard deviation in etch figure diameter of all specimens observed in this study. Right: Xe-irradiated Otter Lake (10-10) annealed at 380 °C; this sample showed the second greatest etch figure standard deviation observed in this study. Lower left: Au-irradiated Durango (2-1-10) annealed at 380 °C, showing etch figure diameter variability. Scale bar shown in the upper left applies to all images.

Table 5: Etch figure diameters, standard deviations, and standard error (error of the mean) for Xe-irradiated specimens, reported as a function of temperature, apatite composition, and orientation.

Sample	Annealing Temperature (°C)	Tracks Observed?	Diameter (μm)	Standard Deviation (μm)	Standard Error (μm)
Durango (10-10)	unannealed	yes	CNBD		
	320	yes	CNBD		
	340	N/A			
	360	yes	CNBD		
	380	no			
	400	no*			
	420	no*			
Otter Lake (10-10)	unannealed	yes	CNBD		
	320	N/A			
	340	yes	2.25	0.16	0.02
	360	N/A			
	380	yes	2.29	0.58	0.08
	400	no*			
	420	no*			
Durango (2-1-10)	unannealed	N/A			
	320	yes	CNBD		
	340	yes	CNBD		
	360	yes	CNBD		
	380	yes	CNBD		
	400	no			
	420	no			
Durango (10-11)	unannealed	yes	CNBD		
	320	yes	CNBD		
	340	yes	CNBD		
	360	yes	CNBD		
	380	yes	CNBD		
	400	no			
	420	no			
Durango (0001)	unannealed	yes	CNBD		
	320	yes	CNBD		
	340	yes	CNBD		
	360	yes	CNBD		
	380	yes	CNBD		
	400	no*			
	420	no			

Otter Lake (0001)	unannealed	yes	CNBD		
	320	yes	CNBD		
	340	yes	CNBD		
	360	N/A			
	380	yes	CNBD		
	400	no			
	420	no			
				*anomalous streaks observed	
			CNBD = could not be determined, due to overlapping tracks		

.

As noted in Tables 4 and 5, anomalous streaks were observed on some Durango (10-10), Durango (2-1-10), Durango (0001), and Otter Lake (2-1-10) specimens annealed in the temperature range 380-420 °C. These streaks, shown in Figure 21, are parallel and resemble etch figures, except they are oval-shaped with no evident hexagonal symmetry, and have a very wide distribution in lengths (~2-20 μm). As can be seen, the streak morphology, sizes, and size distributions are somewhat different between samples. Durango (0001) and Otter Lake (10-10) streaks generally have a more oval-shaped morphology with wider length distribution, while Durango (2-1-10) and (10-10) have a more rod-shaped morphology with a narrower size distribution. For only one specimen – Otter Lake (10-10) – were streaks observed on specimens irradiated with both Au and Xe ions. For these specimens, no difference in streak morphology was observed, suggesting that streak morphology is not function of irradiation ion or fluence. No streaks were observed on samples annealed below 380 °C. In addition, no streaks were observed on samples that showed etch figures, suggesting that streak formation occurs above annealing temperatures. Note that the (0001) face is perpendicular to the c-axis, so these streaks do not reflect c-axis elongation. In most cases, polishing scratches are extremely diffuse, sometimes completely absent due to extensive annealing. However, the Otter Lake (10-10) streaks appear to nucleate on a prominent polishing scratch. Also noticeable is an increased surface roughness of some samples showing streaks relative to samples annealed at lower temperatures (compare Figs. 13, 18, 19, 20, 21).
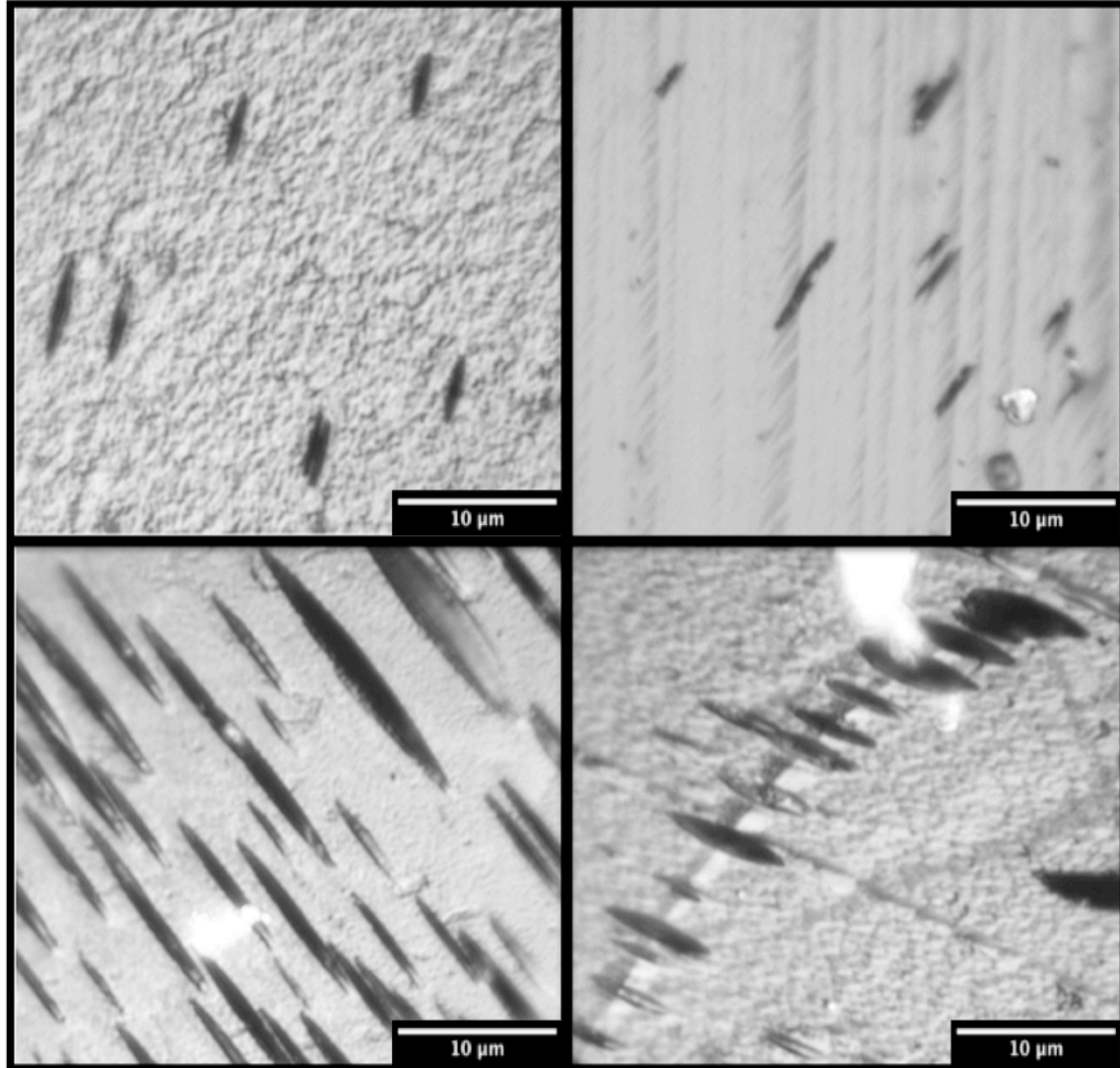
Figure 21: Representative photomicrographs of specimens that showed anomalous streaks after annealing in the range 380-420 °C and etching. Each sample shown here was annealed at 400 °C. Top row: Au-irradiated Durango (10-10) (left) and Durango (2-1-10) (right), showing streaks with rod-like morphology and uniform length. Bottom row: Xe-irradiated Durango (0001) (left) and Otter Lake (10-10) (right), showing longer streaks with oval-like morphology and wider size distribution.

3.3 SAXS and AFM: latent (unetched) tracks

Small Angle X-ray Scattering

A CCD image of a SAXS pattern collected from a Durango (10-10) specimen is shown to the left in Figure 22. The image of X-rays scattered by the cylindrical nanometer-sized latent tracks can be clearly seen. To the right, Figure 22 shows the oscillating scattering intensity plotted as a function of the scattering vector, q. Solid lines show the calculated intensity oscillations, assuming a hard cylinder track

40

model. The calculated and measured oscillation patterns are in close agreement, confirming the geometry of the latent FTs. Mean track diameters and standard deviations as determined by SAXS measurements are summarized in Table 6 and are displayed graphically in Figure 23. The range of radii for different apatite compositions and orientations was 4.78-4.94 nm, indicating a very similar track size for all samples. However, given the exceptional accuracy of the SAXS measurements (one-sigma ~0.01-0.02 nm), subtle changes in track diameters are statistically significant. The track size depends systematically on the orientation of the track to the *c*-axis (Fig. 23). Diameters for (0001) tracks are 4.92 and 4.85 nm for Otter Lake and Durango, respectively, while diameters of (10-10) tracks are 4.81 nm for both compositions. In addition, track diameter varies as a function of chemistry, with tracks from the Otter Lake apatite having larger diameters than those from the Durango apatite, except for tracks in the (10-10) orientation, which showed identical mean track diameters for both Otter Lake and Durango specimens (Fig. 23).
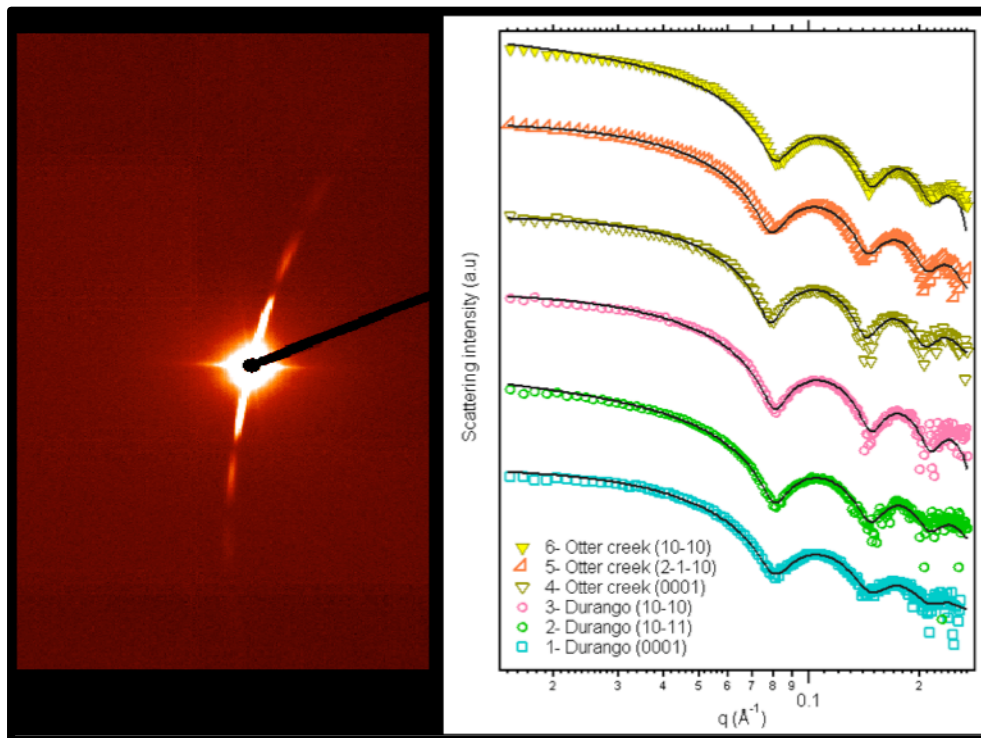
Figure 22: Left: An experimental SAXS diffraction image collected for the Otter Lake (10-10) specimen irradiated with 2.2 GeV Au ions. Right: X-ray scattering intensities as a function of scattering vector, *q*, which are well described by the calculated intensities using the hard cylinder track model (solid curves).
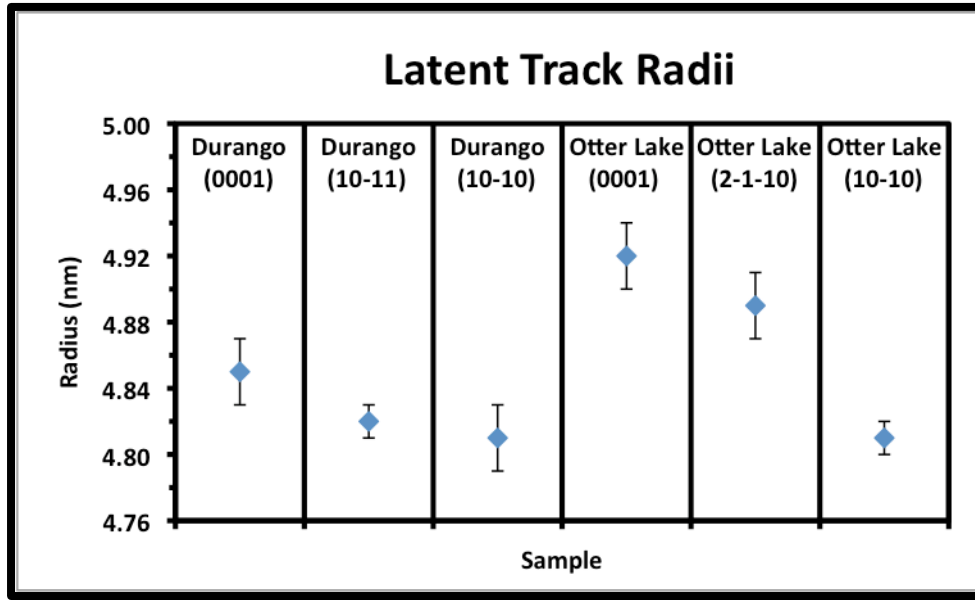
Figure 23: Latent track radii of 2.2 GeV Au-irradiated samples, as determined by the fitted track models to the SAXS data, shown in Figure 22. The tracks in the Otter Lake apatite generally have larger radii than those in the Durango apatite, and the (0001) orientations have larger radii than other orientations. Error bars are for one-sigma.

Table 6: Summary of latent track diameters as a function of apatite composition and orientation, as recorded by SAXS for 2.2 GeV Au-irradiated samples. These data are plotted in Figure 23.

Sample	Radius (nm)	Standard Deviation (nm)
Durango (0001)	4.85	0.02
Durango (10-11)	4.82	0.01
Durango (10-10)	4.81	0.02
Otter Lake (0001)	4.92	0.02
Otter Lake (2-1-10)	4.89	0.02
Otter Lake (10-10)	4.81	0.01

Atomic Force Microscopy

AFM analysis revealed the presence of hillocks on the irradiated surfaces of 5 of 8 samples, and representative images are shown in Figure 24. The mean hillock heights and diameters with standard deviations are also given in Figure 24, as well as Table 7. The hillock densities are generally consistent with the radiation fluence, confirming that the features are in fact irradiation-induced hillocks. The data presented here represent hillocks measured with two AFM probes. This is because tips degraded with use and had to be changed regularly, such that all samples could not be analyzed with the same probe. While measured hillock diameters are significantly different between samples measured with probes 1 2, specimens analyzed with the same probe show relatively similar diameters to one another.

This suggests that quantitative comparison cannot be made between samples analyzed with different probes. This is logical since tip radius is likely to vary from probe to probe. Both specimens analyzed with probe 2 are *c*-axis parallel, and of them the Otter Lake hillocks have greater diameters. Of the three specimens analyzed with probe 1, Otter Lake hillocks are also wider. In addition, diameter decreases with increasing angle of the track to the *c*-axis. Hillock heights, on the other hand, show no systematic dependence on the tip used for analysis, and they do not show any apparent composition or orientation dependences.
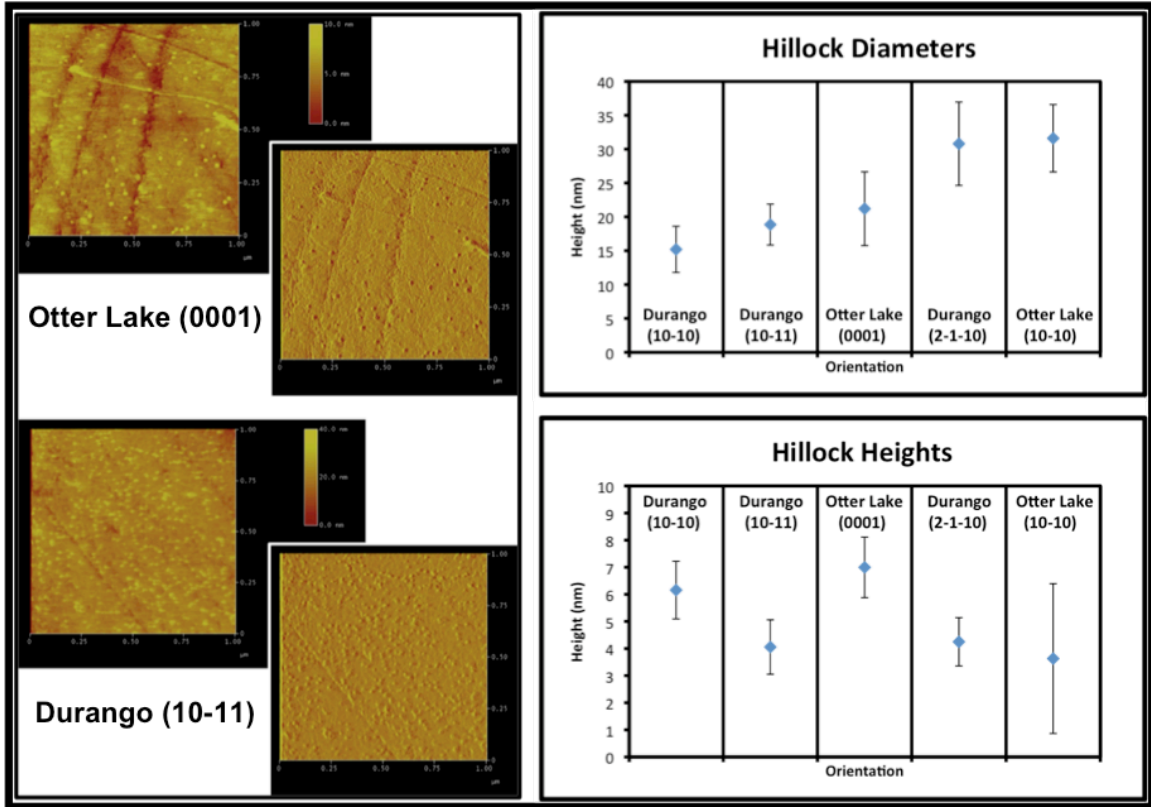
Figure 24: Left: AFM images showing hillock formation on apatite surfaces irradiated with 185 MeV Xe. In each pair, the upper left image shows height variation, and the lower right image shows tip deflection. Image area is 1 μm². Right: Hillock diameters (top) and heights (bottom) from each sample on which hillocks were observed. For both graphs, the three data points to the left were collected with the same probe, and the two data points to the right were collected with a different probe. Error bars are for one-sigma.

Table 7: Hillock diameters and heights for 185 MeV Xe-irradiated samples, reported as a function of orientation, and displayed graphically in Figure 24.

Sample	Probe	Average Diameter (nm)	St. Dev. (nm)	Avgerage Height (nm)	St. Dev. (nm)
Durango (10-10)	1	15.20	3.41	6.16	1.06
Durango (10-11)	1	18.86	3.03	4.06	1.00
Otter Lake (0001)	1	21.20	5.45	7.00	1.12
Durango (2-1-10)	2	30.80	6.16	4.25	0.89
Otter Lake (10-10)	2	31.61	4.97	4.97	2.76

4. Discussion

4.1 Etched tracks

The general relation between annealing temperature and track orientation observed in this study is consistent with observations of other studies. For both apatite compositions, (0001) etch figures were observed at higher temperatures than other orientations (Table 4, Figure 17). This observation is consistent with several studies that report slower annealing rates with decreased angle between the track and the *c*-axis (Donelick, 1991, Donelick et al., 1999; Donelick and Miller, 1991; Ketcham, 2003; Vrolijk et al., 1992). This is due to preferential diffusion of defects that constitute the amorphous track in the *c*-axis direction during annealing, resulting in preservation of tracks that run parallel to the *c*-axis, while tracks running perpendicular to the *c*-axis become segmented, as shown in Figure 25 (Chadderton, 1988, Gleadow et al., 2002, Green and Durrani, 1977; Li et al., 2011, Mrowec, 1980). The preferred *c*-axis-parallel diffusion is due to the channeled structure of apatite along the *c*-axis (Fig. 1) (Hughes et al., 1990). Similar behavior was reported by Stormer et al. (1993) for F and Cl diffusion, explaining the anomalous EPMA results for apatite specimens bombarded normal to the (0001) plane. Afra et al. (2011) and Green et al. (1986) report complete annealing at 400 °C for 30-minute and 20-minute annealing runs, respectively. Thus the significant decrease in diameter and extreme (> a factor of three) increase in standard deviation for the Durango (0001) samples observed at 400 °C – the only samples in this study observed at 400 °C – reflect near-annealing of tracks.
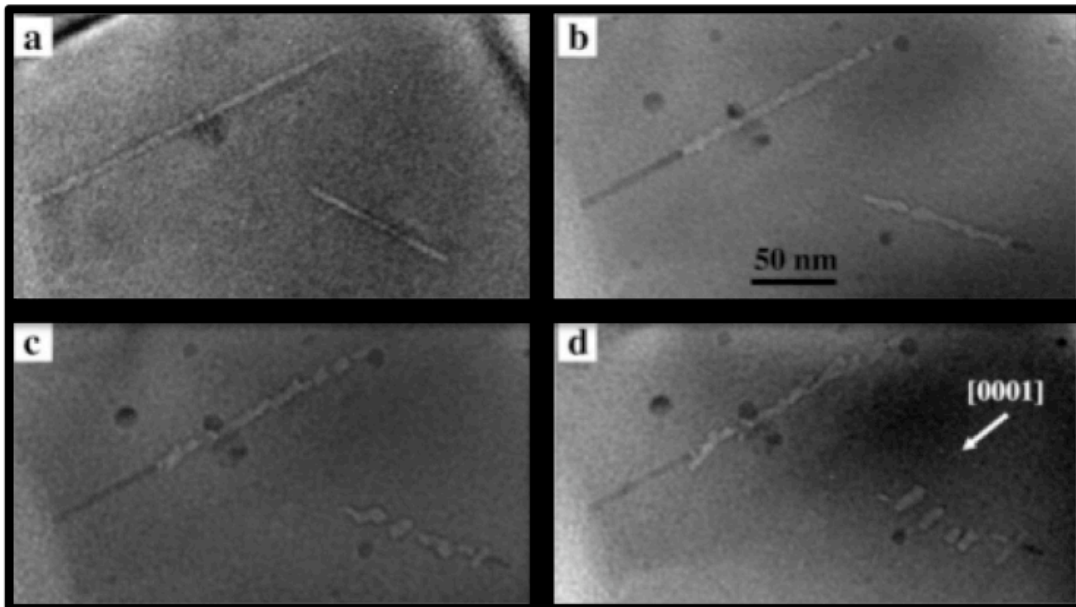
Figure 25: TEM images showing enhanced segmentation of non-*c*-axis-parallel tracks relative to *c*-axis parallel tracks, due to diffusion of track material (defects) in the *c*-axis direction during annealing. Tracks are shown (a) before annealing, (b) after 1, (c) 17 and (d) 60 minutes of annealing at 700°C. Figure from Li et al. (2011).

Green et al. (1986) presented data on Durango apatite annealed for 20-minutes at temperatures in the range 95-400 °C. After annealing, etched tracks showed 50% shortening – from 16 μm to 8 μm – at approximately 370 °C: whereas, complete track length reduction – from 8 μm to 0 μm – was observed at 370-400 °C (Fig. 4). Green et al. (1986) described this behavior as "accelerated length reduction" over temperatures 370-400 °C and suggested that crystalline gaps, as described in the Introduction, may have become large enough that they are not removed during etching, resulting in sudden, distinct truncation of etchable track lengths.

The reduction in etch figure diameter observed in this study – with accelerated reduction in the range 360-400 °C – shows a similar trend as track lengths reported in Green et al. (1986). These similar observations suggest that track length reduction and etch figure reduction are linked. Since samples used in this study were prepared for viewing from the surface, observation of track lengths was not readily possible. An attempt was made to re-polish samples from the side, but due to the thinness of the samples and the brittle nature of apatite, this was not possible. However, the higher-than expected irradiation fluence for the Xe-irradiated samples provided large enough features that, despite the surface roughness, some tracks could be viewed in cross-section. Unannealed Durango (10-11) apatite Xe tracks after 30 s and 90 s of etching are shown in transmitted light in Figure 26. Tracks after 30 s of etching appear to be approximately 12 μm long. The darker contrast in the image taken after 90 s of etching is likely due to the greater track diameters relative to the 30 s image, such that the projected track images blur together. Nevertheless, the ends of a few tracks can be seen, and it is clear that the tracks after 90 s of etching are shorter than the same tracks after 30 s of etching by approximately 1-2 μm. Furthermore, SRIM calculations predict 14.8-μm latent track lengths for the Xe irradiations in this study (Ziegler et al., 2010). Given the 12 μm length observed after 20 s of etching, it is possible that track shortening began even before 30 s. Track shortening during etching seems contradictory, since tracks are enlarged during etching. Indeed, track length does increase as amorphous material is removed during etching. However, once all amorphous material is removed, because etchant concentration is greater at the surface of the mineral specimen than at the inner tip of the IT, etch rates at the surface are faster than at the inner tip of the track. This concentration gradient is due to diffusion limitations within the track. As Villa et al. (1997) notes,

> "The concentration of the acid solution decreases within the track, and its partial renewal is ensured by the parent solution. A diffusive phenomenon can express a renewal at the opening that is faster than the renewal at the bottom of the track, as well as an increase in renewal over time."

Thus it is likely that amorphous material was removed from the track after only the first few seconds of etching, after which track lengths began to decrease.
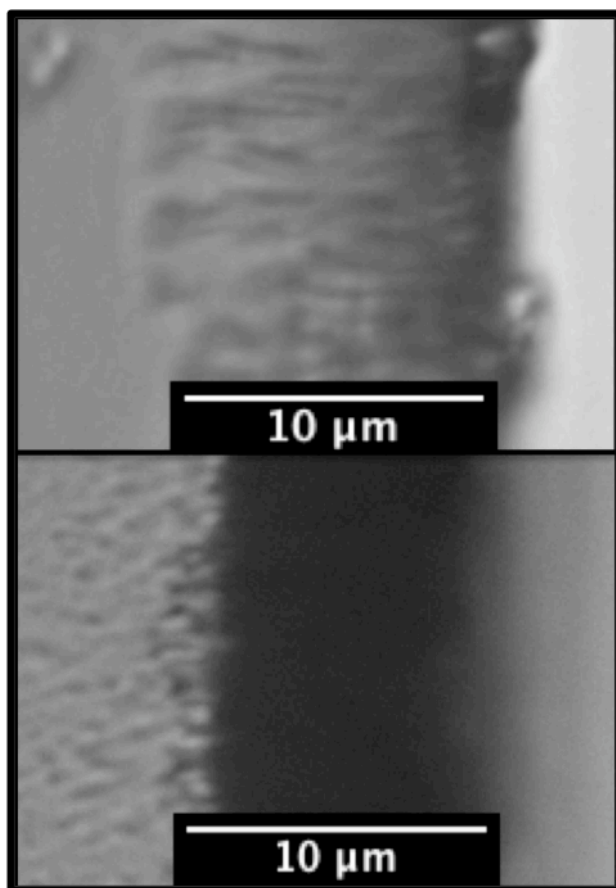
Figure 26: Unannealed Durango (10-11) tracks after etching for 30 s (top) and 90 s (bottom), showing decrease in track length as a function of etching time, due to diffusion-limited etch rates at the end of the track relative to etch rates at the surface.

        The effect of track shortening on etch figure diameter can be understood using simple geometry. Since tracks etch from the surface inward, the crystalline material surrounding the track nearer to the surface experiences more etching than the material deeper into the apatite, resulting in a conical geometry. This effect is enhanced by the diffusion-limited etchant concentration gradient discussed above. Shorter tracks have higher conic angles (e.g. Fleischer 2004, 1981). Since all tracks shorten with increased etching time, tracks with higher conic angles have greater susceptibility to etch figure diameter reduction due to the greater taper of the track (Fleischer and Hart, 1972). Since, as reported by Green et al. (1986), annealed tracks have shorter lengths and therefore higher conic angles, annealed tracks may show greater etch figure diameter decrease during etching. This phenomenon is illustrated in Figure 27. Assuming conic angle remains constant throughout etching, decrease in etch figure diameter relative to a hypothetical, infinitely-long track can be calculated. Assuming the hypothetical track would have an etch figure diameter of 2 μm, and assuming 1.5 μm of track shortening occurs during etching, etch figure diameter reduction can be calculated by the following equation:

etch figure diameter reduction (μm) = 1.5*2*tan(conic angle), where

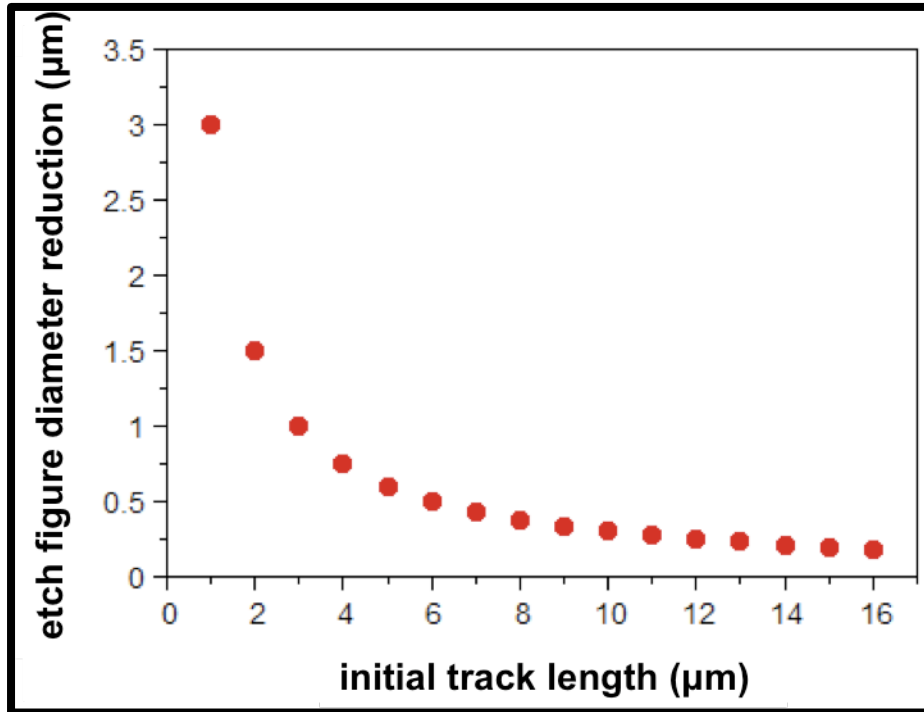conic angle (°) = 2*tan^{-1}($^{1\,\mu m}/_{\text{track length}}$).

Shown in Table 8 are the results of these calculations. Etch figure diameter reduction is plotted graphically in Figure 28.
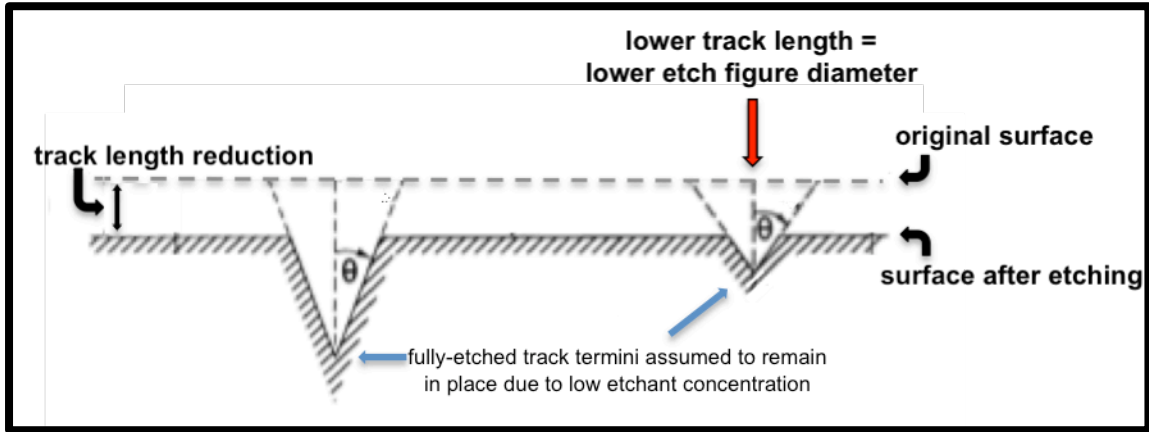
Figure 27: Schematic diagram showing the relative reduction in etch figure diameter as a function of track height – and the directly related parameter conic angle – due to track shortening via surface etching after amorphous material is removed from the track. Figure adapted from Fleischer (1981).

Table 8: Etch figure diameter reduction relative to an infinitely long track with conic angle 0, resulting from 1.5 μm track shortening due to surface etching, assuming a constant conic angle and a 2 μm etch figure diameter for the infinitely long track. These data are plotted in Figure 28.

initial track length (μm)	conic angle (°)	etch figure diameter reduction relative to infinitely-long track with conic angle 0 (μm)
16	7.15	0.19
15	7.63	0.20
14	8.17	0.21
13	8.80	0.23
12	9.53	0.25
11	10.39	0.27
10	11.42	0.30
9	12.68	0.33
8	14.25	0.38
7	16.26	0.43
6	18.92	0.50
5	22.62	0.60
4	28.07	0.75
3	36.87	1.00
2	53.13	1.50
1	90.00	3.00

Figure 28: The relation between initial track length and etch figure diameter reduction, relative to an infinitely long track, due to track length reduction from surface etching after all amorphous material within the track is removed. The data points correlate with values shown in Table 8. See Table 8 caption and text for calculation details.

Table 8 and Figure 28 show that as track length decreases, conic angle increases very slowly at first, resulting in only marginal differences in etch figure diameter decrease. However, as track length decreases further, etch figure diameter reduction accelerates. The observation by Green et al. (1986) of 50% shortening from 16 μm to 8 μm for 20-minute annealing times at 370 °C, according to Table 8 would result in an etch figure diameter reduction of

 0.38-0.19 = 0.19 μm.

Since the etch figure diameter of a 16 μm-long track would be 1.81 μm (2.00 μm – 0.19 μm), this represents only a 10% decrease in etch figure diameter. Etch figure diameter reduction begins to accelerate when track lengths are reduced to ~6 μm. For example, according to this model, a 5-μm long track would show an etch figure reduction of

0.60-0.19 = 0.41 μm,

relative to an unannealed (16-μm long) track. This is a two-fold greater reduction than would result from an 8-μm long track. A 3-μm long track, on the other hand, would show yet another two-fold greater etch figure diameter reduction (0.81 μm). Since accelerated etch figure reduction is associated with tracks of 6 μm or less, the suggestion of Green et al. (1986) that accelerated length reduction begins when

tracks reach 8 μm length explains why the acceleration in etch figure diameter decrease observed in this study was more somewhat more sudden, occurring within a 20 °C temperature window in some cases, than the length reduction of Green et al. (1986). Specifically, since track length and etch figures reach 0 at approximately the same time (complete annealing), the temperature window for accelerated etch figure reduction is narrower than that of accelerated length reduction.

Given the suggestion by Green et al. that crystalline gap formation begins to occur after track lengths are reduced to ~8 μm, accelerated etch figure reduction coincides with gap formation. Also, given the suggestion by Green et al. (1986) that gaps may be unetchable, resulting in random shortening of track lengths, the increased variation in etch figure diameter is expectable, since Table 8 and Figure 28 show that etch figure reduction varies widely with small variations in track length in the range 0-6 μm.

A similar relation between etch figure diameter and degree of annealing was observed by Storzer and Wagner (1969) in laboratory-annealed Australian tektite. In that study, track lengths were not measured but rather track densities, with decreased density representing increased annealing extent. Figure 29 summarizes the observations of Storzer and Wagner (1969). The behavior is analogous to that observed for apatite in this study. Also shown is a window of accelerated etch figure diameter decrease associated with track densities below a threshold density decrease of approximately 60%. Since 6 μm apatite fission tracks represent 63% track shortening, the model presented in Table 8 and Figure 28 is consistent with the observations of Storzer and Wagner (1969). Since apatite and tektite are very different materials, this correlation suggests that the geometric principles used to derive Table 8 may apply reasonably well to tracks in a variety materials. The decrease in etch figure diameter observed by Wagner and Storzer (1969) is generally more gradual than the diameter decrease reported in this study. This is likely because Wagner and Storzer (1969) used isothermal annealing experiments, while this study used isochronal annealing experiments. Given the greater sensitivity of annealing rates to temperature than time, etch figure diameter decrease would be expected to be more sudden in this study than in Wagner and Storzer (1969).
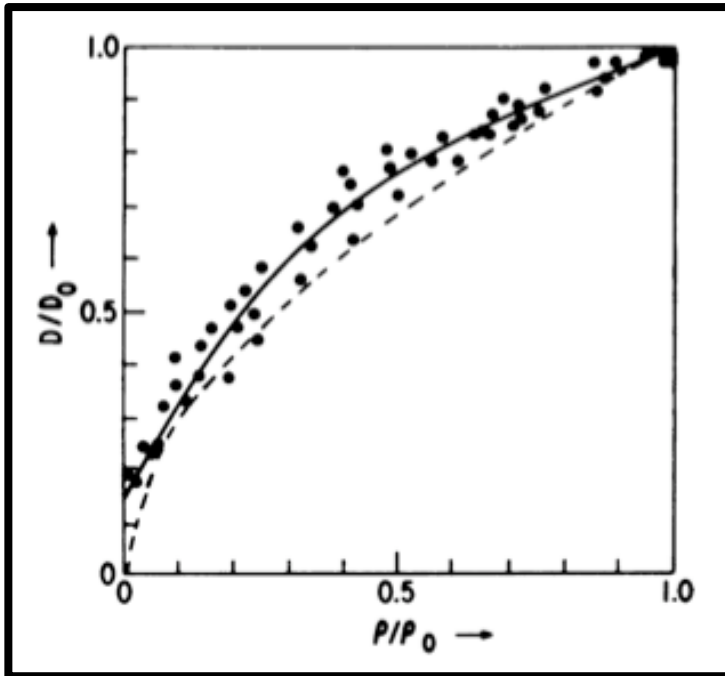
Figure 29: The relation between etch figure diameter and track density observed in a laboratory annealing experiment on Australian tektite by Storzer and Wagner (1969). The vertical axis is the diameter reduction normalized to unannealed track diameters, and the horizontal axis is the track density reduction normalized to unannealed track densities. Shown is a gradual length reduction with annealing, followed by an accelerated length reduction for greater annealing times.

Despite the success of Table 8 and Figure 28 in explaining the acceleration in etch figure diameter reduction, the calculated reductions between 16 μm tracks and 8 μm tracks is in general greater than the differences observed in this study. This is because the model represented in Figure 28 is an oversimplification, not taking into account the diffusion-related changes of the conic angle as a function of etching time. That is, regions closer the surface are likely to experience faster etching rates than regions nearer the track tip, and so conic angle should increase with etching time, resulting in less etch figure diameter reduction than are reported in Table 8, more similar to the experimental observations in this study.

A complementary explanation for the relatively lower etch figure diameters observed for shorter, more annealed tracks can be understood in terms of simple crystallographic constraints. Due to the conical morphology of etched tracks, track widening at the surface must be accommodated by track widening at all points below the surface, down to the track tip, at which the track diameter is 0. Since for shorter tracks, this point of zero width is closer to the surface, shorter tracks have greater constraints on widening, and therefore may have lower etch figure diameters even before the onset of track shortening. Stated another way, due to the conical morphology of tracks, as etch pits widen after amorphous material is removed, they experience etching not only in the radial direction, but also in the vertical (track-length) direction. Due to their greater tapers, for any given amount of radial widening, shorter tracks must experience greater amounts of vertical etching. Therefore, track diameters should increase more slowly upon etching for shorter tracks than for longer tracks. This model would result in complementary behavior to the geometric model discussed above (Table 8). However, while the model discussed above applies only after amorphous material is removed and tracks begin to shorten, the latter model applies throughout the entire etching process.

51

Despite their assumptions and inherent flaws, the models presented here illustrate the general nature of the relation between etch figure diameters and etched track lengths. More detailed models should be developed, and these should take into account etchant concentration gradients and etchant diffusion, while allowing for conic angle increase throughout etching. In addition, such models should be applied to different crystallographic orientations and different apatite compositions. If such models can be developed, these likely will explain more accurately the diameter variations observed in this study as a function of apatite composition, orientation, and annealing temperature.

An alternate explanation for track diameter reduction and variability may be the formation of large crystalline gaps at the very near surface. If, as assumed earlier, 1.5 μm of surface material removal occurs during etching, a gap that forms within the upper 1.5 μm of the surface will be breached during etching. After the gap is breached, the amorphous material beneath begins to be etched. If the gap is sufficiently large, etching of the material below will be significantly delayed, resulting in reduced etch track diameters. Since etch track diameter increases linearly with time, etch figure diameter will decrease linearly with the depth of the gap. However, one potential problem with this explanation is the observation by Li et al. (2012) that IT annealing is negligible in the near-surface region of the track (see Fig. 7 and caption). However, it is obvious that at some point during the annealing process, track diameters near the surface must decrease and gaps must form. Therefore this explanation may apply to the specimens observed at the very latest stages of annealing. This may help to explain the extreme increase in standard deviation of etch figure diameters observed for the Durango (0001) sample annealed at 400 °C, because, as remarked above, this sample was likely very close to the annealing threshold.

4.2 Latent track relation to etched track morphology

The latent track diameters measured by SAXS are consistent with other studies using both TEM and SAXS. The SAXS study of Afra et al. (2011) shows identical track diameters. TEM studies, on the other hand, show similar mean diameters but greater variation, in the range ~5-13 nm (Li et al., 2011; Paul and Fitzgerald, 1992). Despite the greater variation in diameters, however, TEM studies report the same orientation dependence as was observed in this study, with tracks having lower angles to the *c*-axis showing higher diameters. This orientation dependence could not be compared with other SAXS results because previous SAXS studies have not considered orientation.

The observation of hillocks in apatite by AFM has not been reported previously. The lack of hillocks on 3 of the 8 samples is inexplicable at this point. For the 5 samples that showed hillocks, observation of hillocks was never immediate upon the commencement of scanning, instead requiring adjustment of scan parameters such as deflection setpoint and integral gain, moving the tip to different areas of the specimen, or changing the probe. Thus it is likely that hillocks indeed exist on all 8 samples, but during AFM scanning, in only 5 cases was the combination of tip quality, scanning parameters, and specimen area adequate to

result in hillock observation. Lang et al. (2002) reported hillock formation from ITs induced by the same ions and energies as used in this study (185 MeV Xe) on the basal planar surface of phlogopite. The average hillock diameters and heights reported therein were 12.5 nm and 0.8 nm, respectively. These dimensions are significantly smaller than those of apatite in this study (15-30 nm and 3-7 nm). Comparing the AFM results to the SAXS measurements, hillock diameters were 1.5-3 times larger than latent track diameters determined by SAXS. Zhang et al. (2009) imaged both track diameters within the host mineral as well as hillock diameters at the surface of $Gd_2Zr_2O_7$ pyrochlore irradiated with 12-MeV C_{60} clusters and reported no significant difference in track and hillock diameters. Thus the difference in latent track and hillock diameters in this study may be due to error in the AFM measurement.   However, hillock diameters showed the same orientation dependence as latent tracks measured with SAXS and TEM, discussed above. In addition, AFM showed the same composition dependence as SAXS results. This suggests that, despite the possible exaggeration of absolute track dimensions using AFM, relative dimensions are accurate.

The relative diameters of latent tracks as a function of orientation and composition not only agree between AFM and SAXS measurements, but the trends are visible in etched tracks as well (Figs. 13, 17). This suggests that a relation may exist between etch figure diameters and latent track sizes.   For example, characteristics that control damage production, such as directional bond strength, may also control etch rates. However, the agreement between latent track and etch figure diameters is not perfect. Both SAXS and AFM show that latent track radii and hillock dimensions decrease monotonically with increasing angle between the track and the *c*-axis, in agreement with the known monotonic trend of decreased annealing rates with track angle to the *c*-axis, discussed above (Donelick, 1991, Donelick et al., 1999; Donelick and Miller, 1991; Ketcham, 2003; Vrolijk et al., 1992). However, etch figure diameters show a reverse trend, with (10-11) etch figures (which are 45° to the *c*-axis) having lower diameters than both *c*-axis-parallel and *c*-axis-perpendicular etch figures. This non-monotonic trend as a function of track angle to the *c*-axis suggests etch rates may have more complex controls than damage production and annealing behavior.

The lack of correlation between hillock heights and diameters is inexplicable. Given the similarity in latent track and hillock diameters as determined by SAXS and AFM, respectively, there is no apparent reason that hillock heights should show significant scatter. Thus hillock height determination using AFM may simply be unreliable.

4.3 Relevance to fission track dating

This study shows that the variation in D_{par} measurements observed in natural specimens (Donelick, 1993; Donelick et al., 2005) may be due to the different amounts of annealing experienced by natural FTs, since each has a different age. At first glance, the geometric model used in this study to explain this variability seems not to apply to FT-dating, since the model explained etch figure reduction as a function of track shortening due to over-etching, while FT-dating

laboratories take careful precautions to avoid over-etching. However, track lengths are measured from confined FTs, not FTs that intersect the surface. In fact, FTs that intersect the surface are used as conduits for etchant to reach the confined tracks. Due to the diffusion-related etchant concentration gradient reported by Villa et al. (1997) and discussed above, the effective etchant concentration within the confined track is certainly lower than the concentration in the track intersecting the mineral surface. Therefore, when confined tracks are fully etched, surface-intersecting tracks (i.e. those used for D_{par} measurement) are certainly over-etched, resulting in track shortening. Thus the geometric model in Table 8 and Figure 28 applies.

While this potential variability in D_{par} measurements cannot be avoided with natural specimens, the relation between etch figure diameters and etch figure lengths suggests that there are some appropriate safeguards to consider. Specifically, by comparing etch figure diameter with etched track length, anomalously low D_{par} values may be avoided simply by not using those values derived from tracks with lengths below a certain threshold, such as 6 μm. If an accurate model of the relation between track length and etch figure diameter can be developed, based on diffusion and accounting for the increase in conic angle with etching time, it is possible to correct anomalously low D_{par} values by extrapolation back to longer track lengths. Because in many cases only a few D_{par} values are observed on natural specimens (Donelick, 1993), such a correction may significantly improve the accuracy and precision of the D_{par} kinetic proxy.

One important criticism of the use of D_{par} as a kinetic parameter has become evident from this work: D_{par} fails to predict the relative kinetics between Otter Lake and Durango apatite. Larger etch figure diameters were observed for Otter Lake relative to Durango apatite, yet Durango tracks were observed at slightly higher temperatures than Otter Lake tracks. This was evidenced by the presence of etch figures on the Durango (0001) and (2-1-10) orientations at one temperature higher than the Otter Lake (0001) and (2-1-10) orientations. This is the opposite trend to that expected when using D_{par} as a kinetic proxy, which correlates lower etch figure diameters with faster annealing kinetics. This same contradiction is evident in the results of Ravenhurst et al. (2003) as well. The failure of D_{par} as a kinetic parameter in some situations has been recognized by the FT-dating community (Donelick, 1993; Donelick et al., 2005). Donelick et al. (2005) attribute the failure to variations in apatite chemistry, most notably high OH-content.   OH-content was not determined directly in this study, but the high F-content of both Durango and Otter Lake apatite indicate that OH-content is low for both. However, the high Si- and CO_2-contents in Otter Lake relative to Durango apatite, as well as the anomalously high F-content of Otter Lake apatite, suggest that etching rates may have subsidiary chemical controls other than Cl-content. Because the Cl-content is low in both the Durango and Otter Lake apatite relative to the range of apatite compositions in nature (Carlson et al., 1999), it is possible that these subsidiary chemical controls may have had greater relative effect than is commonly appreciated in natural apatite, reducing the efficacy of the D_{par} parameter.

Another observation from this study that has great relevance to the FT-dating community is the two-fold greater discrimination between Durango and Otter Lake apatite based on (10-11) etch figures relative to (10-10) etch figures.

This implies that the resolution of kinetic proxies can be greatly increased by using (10-11) etch figures in addition to the (10-10) etch figures currently used for D_{par} measurement. Use of etch figures on the (10-11) growth face would increase the etch figure sample size as well.

4.4 Anomalous Streaks

The observation of anomalous streaks (Fig. 21) in various samples annealed at temperatures of 380 °C and higher is as of yet inexplicable. Etch figures and streaks were never observed on the same specimen, indicating that the streaks are associated with temperatures above the annealing threshold. Specimens showing streaks were washed with acetone to ensure that the streaks did not simply result from surface contamination. However, streaks were still present after washing. Specimens showing streaks were examined in cross section to look for evidence of tracks, but no tracks were observed. Because these samples were annealed at 450 °C for 24 hours prior to irradiation, it is unlikely that streaks were due to structural or surface changes induced by high annealing temperatures. The observation of streak nucleation on a large polishing scratch for the OL (10-10) sample suggests that they may be related to surface defects. On the other hand, observation of rough surface texture on some streaked samples suggests that they may be associated with surface recrystallization during annealing.

5. Conclusions

Ion track etch figures in apatite decrease in size as a function of increasing temperature, showing an accelerated decrease in diameter as the temperature approaches the annealing threshold. Associated with this decrease in etch figure diameter is an increase in etch figure diameter variability, with one standard deviation being as large as 40% of the mean etch figure diameter. Extrapolation of these results to geological time and temperature scales explains the variation in D_{par} measurements reported in the FT-dating literature. The relation between track length reduction and annealing temperature is supported by a simple geometric model and suggests that anomalously low D_{par} measurements may be corrected by comparison of etch figure diameters and track lengths. However, for accurate correction, more detailed models of etch figure reduction with annealing time and temperature must be developed.

The observed factor of two increase in the difference etch figures on the (10-11) growth face as compared with (10-10) etch figures currently used for kinetic proxy measurements suggests that the use of (10-11) etch figure measurement in the FT dating method could improve the resolution of kinetic proxies, in addition to increasing etch figure sample size, improving the accuracy of kinetic proxies.

The relation between latent track morphology, annealing behavior, and etch rates suggests that damage production, etching behavior, and annealing processes are controlled by the structure of the material, although etching behavior may show additional controls, as evidenced by the non-monotonic relation between etch pit diameter and angle relative to the c-axis. The agreement between the AFM and SAXS results regarding track and hillock diameters provides confidence in the value of these techniques, suggesting they may be used in addition to TEM studies to investigate latent tracks.

Finally, the observation of anomalous streaks on the surfaces of samples annealed at 400-420 °C is presently inexplicable. Possible explanations include the possibility of a high-temperature surface reaction during annealing or interactions of etchant with surface defects, such as polishing scratches.

6. Acknowledgements

7. References

Afra, B., Lang, M., Rodriguez, M., Zhang, J., Giulian, R., Kirby, N., Ewing, R.C., Trautmann, C., Toulemonde, M., Kluth, P., 2011. Annealing kinetics of latent particle tracks in Durango apatite. Phys. Rev. B 83(6), 1-5.

Barbarand, J., Hurford, T., Carter, A., 2003a. Variation in apatite fission-track length measurement: implications for thermal history modelling. Chem. Geol. 198(1-2), 77-106.

Barbarand, J., Carter, A., Wood, I.,Tony, H., 2003b. Compositional and structural control of fission-track annealing in apatite. Chem. Geol. 198(1-2), 107-137.

Bhandari, N., Bhat, S.G., Lal, D., Rajagopalan, G., Tamhane, A.S., Venkatavaradan, V.S., 1971. Fission fragment tracks in apatite: Recordable track lengths. Earth Planet. Sci. Lett. 13, 191-199.

Burtner, R.L., Nigrini, A., Donelick, R.A., 1994. Thermochronology of Lower Cretaceous source rocks in the Idaho-Wyoming thrust belt. AAPG Bullet. 78 (10), 1613-1636.

Carlson, W.D., 1990. Mechanisms and kinetics of apatite fission-track annealing. Am. Mineralog. 75, 1120-1139.

Carlson, W.D., Donelick, R.A., Ketcham, R.A., 1999. Variability of apatite fission-track annealing kinetics: I. Experimental results, Am. Mineralog. 84, 1213-1223.

Chadderton, L.T., 1988. On the anatomy of a fission track fragment track. Nucl. Tracks Radiat. Meas. 15, 11-29.

Crowley, K.D., Cameron, M., Schaefer, R.L., 1991. Experimental studies of annealing of etched fission tracks in fluorapatite. Geochim. Cosmochim. Acta 55, 1449-1465.

Donelick, R.A., 1991. Crystallographic orientation dependence of mean etchable fission track length in apatite: An empirical model and experimental observations. Am. Mineralog. 76, 83-91.

Donelick, R.A., 1993. Method of fission track analysis utilizing bulk chemical etching of apatite. Patent 5267274, U.S.A.

Donelick, R.A., Miller, D. S., 1991. Enhanced TINT fission track densities in low spontaneous track density apatite using [252]Cf-derived fission fragment tracks: A model and experimental observations. Nucl. Tracks Radiat. Meas. 18(3), 301-307.

Donelick, R.A., Ketcham, R.A., Carlson, W.D., 1999. Variability of apatite fission-track annealing kinetics: II. Crystallographic orientation effects. Am. Mineralog. 84, 1224-1234.

Donelick, R.A., O'Sullivan, P.B., Ketcham, R.A., 2005. Apatite fission-track analysis. Rev. Mineralog. Geochem. 58(1), 49-94.

Donelick, R.A., Roden, M.K., Mooers, J.D., Carpenter, B.S., 1990. Etchable length reduction of induced fission tracks in apatite at room temperature (~23 °C): crystallographic orientation effects and "initial" mean lengths. Nucl. Tracks Radiat. Meas. 17(3), 261-265.

Dumitru, T.A., 2000. Fission-Track Geochronology. In: Quaternary Geochronology: Methods and Applications. Noller, J.S, Sowers, J.M, Lettis, W.R. (eds). Am.

Geophys. Union Ref. Shelf 4, Washington, DC, American Geophysical Union, 131-155.

Durrani, S.A., Bull, R.K., 1987. Solid State Nuclear Track Detection. Pergamon Press, Oxford.

Fleischer, R.L., 1981. Chapter 4: nuclear track production in solids. Progress in Materials Science "Chalmers Anniversary Volume," 97-123.

Fleischer, R.L., 2004. Fission tracks in solids — production mechanisms and natural origins. J. Mat. Sci. 39, 3901-3911.

Fleischer, R.L., Hart, H.R., 1972. Fission track dating: Techniques and problems. Calibration of Hominoid Evolution, Bishop, W.W., Miller, D.A., Cole, S. (eds). Scottish Academic Press, Edinburgh, 135.

Fleischer, R.L., Price, P.B., Walker, R.M., 1975. Nuclear Tracks in Solids: Principles and Techniques. University of California Press, Berkeley.

Fleischer, R.L., Price, P.B., Walker, R.M., Hubbard, E.L., 1967. Criterion for registration in dielectric track detectors. Phys. Rev. 156, 331-355.

Gallagher, K., Brown, R., Johnson, C., 1998. Fission track analysis and its applications to geological problems. Ann. Rev. Earth Planet. Sci. 26, 519-572.

Gleadow, A.J.W., Duddy, I.R., 1981. A natural long-term track annealing experiment for apatite. Nucl. Tracks Radiat. Meas. 5, 169-174.

Gleadow, A.J.W., Duddy, I.R., Lovering, J.F., 1983. Fission track analysis: A new tool for the evaluation of thermal histories and hydrocarbon potential. Austral. Petrol. Explor. Assoc. J. 23, 93-102.

Gleadow, A.J.W., Belton, D.X., Kohn, B.P., Brown, R.W., 2002. Fission track dating of phosphate minerals and the thermochronology of apatite. Rev. Mineralog. Geochem. 48(1), 579-630.

Gleadow, A.J.W., Duddy, I.R., Green, P.F., Lovering, J.F., 1986. Confined fission track lengths in apatite: A diagnostic tool for thermal history analysis. Contrib. Mineralog. Petrol. 94, 405-415.

Green, P.F., 1988. The relationship between track shortening and fission track age reduction in apatite: combined influences of inherent instability, annealing anisotropy, length bias and system calibration. Earth Planet. Sci. Lett. 89, 335-352.

Green P.F., Durrani, S.A., 1977. Annealing studies of tracks in crystals. Nucl. Track Detection 1, 33-39.

Green, P.F., Duddy, I.R., Gleadow, A.J.W., Tingate, P.R., 1985. Fission-track annealing in apatite: track length measurements and the form of the Arrhenius plot. Nucl. Tracks 10(3), 323-328.

Green, P.F., Duddy, I.R., Gleadow, A.J.W., Tingate, P.R., Laslett, G.M., 1986. Thermal Annealing of Fission Tracks in Apatite; 1. A Qualitative Description. Chem. Geol. 59, 237-253.

Griffith, C., Rossenfeld, C., 2011. "Spontaneous Nuclear Fission," Atomic Archive. 11 July 2012 <http://www.atomicarchive.com/Fission/Fission6.shtml>.

Grivet, M., Rebetez, M., Chambaudet, A., Ben Ghouma, N., 1993. Electron microscopy analysis of krypton ion tracks induced in Durango apatite. Nucl. Tracks Radiat. Meas. 22(1-4), 779-782.

Henderson, C.E., 2011. Protocols and pitfalls of electron microprobe analysis of apatite. M.S. thesis. University of Michigan, Ann Arbor, MI.

Hendriks, B.W.H., Redfield, T.F., 2005. Apatite fission track and (U-Th)/He data from Fennoscandia: An example of underestimation of fission track annealing in apatite. Earth Planet. Sci. Lett. 236(1-2), 443-458.

Hughes, J.M, Cameron, M., Crowley, K.D., 1989. Structural variations in natural F, OH, Cl apatite. Am. Mineralog. 74, 870-876.

Hughes, J.M., Cameron, M., Crowley, K.D., 1990. Crystal structures of natural ternary apatite: Solid solution in the $Ca_5(PO_4)_3X$ (X = F, OH, Cl) system. Am. Mineralog. 75, 295-304.

Jonckheere, R.C., Wagner, G.A., 2000. On the occurrence of anomalous fission tracks in apatite and titanite. Am. Mineralog. 85, 1744-1753.

Kerrick, D.M., Eminhizer, L.B., Villaume, J.F., 1973. The role of carbon film thickness in electron microprobe analysis. Am. Mineralog. 58, 920-925.

Ketcham, R.A., 2003. Observations on the relationship between crystallographic orientation and biasing in apatite fission-track measurements. Am. Mineralog. 88, 817-829.

Ketcham, R.A., 2005. The role of crystallographic angle in characterizing and modeling apatite fission-track length data. Radiat. Meas. 39(6), 595-601.

Ketcham, R.A., Donelick, R.A., Carlson, W.D., 1999. Variability of apatite fission-track annealing kinetics: III. Extrapolation to geological time scales. Am. Mineralog. 84, 1235-1255.

Lal, D., Rajan, R.S., Tamhane, A.S., 1969. Chemical composition of nuclei of Z > 22 in cosmic rays using meteoritic minerals as detectors. Nature 221(January 4), 33-37.

Lang, M., 2001. Rasterkraftmikroskopie an natürlichen und ionen-induzierten strahlenschäden in phlogopit. Diploma thesis. University of Heidelberg, Heidelberg, Germany.

Lang, M., Glasmacher, U.A., Moine, B., Müller, C., Neumann, R., Wagner, G.A., 2002. Heavy-ion induced defects in phlogopite imaged by scanning force microscopy. Surf. Coat. Tech. 158-159, 439-443.

Lang, M., Lian, J., Zhang, F.X., Hendriks, B.W.H., Trautmann, C., Neumann, R., Ewing, R.C., 2008. Fission tracks simulated by swift heavy ions at crustal pressures and temperatures. Earth Planet. Sci. Lett. 274, 355-358.

Laslett, G.M., Kendall, W.S., Gleadow, A.J.W., Duddy, I.R., 1982. Bias in measurement of fission-track length distributions. Nucl. Tracks 6(2), 79-85.

Li, W., Lang, M., Gleadow, A.J.W., Zdorovets, M.V., Ewing, R.C., 2012. Thermal annealing of unetched fission tracks in apatite. Earth Planet. Sci. Lett. 321-322, 121-127.

Li, W., Wang, L., Lang, M., Trautmann, C., Ewing, R.C., 2011. Thermal annealing mechanisms of latent fission tracks: Apatite vs. zircon. Earth Planet. Sci. Lett. 302(1-2), 227-235.

Merlet, C. 1994. An accurate computer correction program for quantitative electron probe microanalysis. Mikrochim. Acta 114/115, 363-376.

Möller, P., Madland, D.G., Sierk, A.J., Iwamoto, A., 2001. Nuclear fission modes and fragment mass asymmetries in a five-dimensional deformation space. Nature 409 (February), 785-790.

Mrowec, S., 1980. Defects and diffusion in solids: An introduction. Elsevier Scientific Publishing, Amsterdam, 466.

Müller, C., Cranney, M., El-Said, A., Ishikawa, N., Iwase, A., Lang, M., Neumann, R., 2002. Ion tracks on LiF and CaF_2 single crystals characterized by scanning force microscopy. Nucl. Inst. Meth. Phys. Res. B 191, 246-250.

Naeser, C.W., 1967. The use of apatite and sphene for fission track age determinations. Geol. Soc. Am. Bull. 78(12), 1523-1526.

Naeser, C.W., 1981. The fading of fission tracks in the geological environment – data from deep drill holes. Nucl. Tracks Rad. Meas. 5, 248-250.

Naeser C.W., Forbes R.B., 1976. Variation of fission track ages with depth in two deep drill holes. EOS, Trans. Am. Geophys. Union 57, 353.

Naeser, N.D., McCulloh, T.H. (eds), 1989. Thermal History of Sedimentary Basins: Methods and Case Histories. Springer-Verlag, Berlin.

O'Sullivan, P.B., Parrish, R.R., 1995. The importance of apatite composition and single-grain ages when interpreting fission track data from plutonic rocks: a case study from the Coast Ranges, British Columbia. Earth Planet. Sci. Lett. 132, 213-224.

Paul, T.A., Fitzgerald, P.G., 1992. Transmission electron microscopic investigation of fission tracks in fluorapatite. Am. Mineralog. 77, 336–344.

Ravenhurst, C.E., Roden-Tice, M.K., Miller, D.S., 2003. Thermal annealing of fission tracks in fluorapatite, chlorapatite, manganoanapatite, and Durango apatite: Experimental results. Canad. J. Earth Sci. 40, 995-1007.

Sandhu, A.S., Westgate, J.A., 1995. The correlation between reduction in fission-track diameter and areal track density in volcanic glass shards and its application in dating tephra beds. Earth Planet. Sci. Lett. 131, 289-299.

Schmidt, K.-H., Steinhäuser, S., Böckstiegel, C., Grewe, A., Heinz, A., Junghans, A.R., Benlliure, J., Clerc, H.-G., de Jong, M., Müller, J., Pfützner, M., Voss, B., 2000. Relativistic radioactive beams: A new access to nuclear-fission studies. Nucl. Phys. A 665, 221-267.

Sobel, E.R., Seward, D., 2010. Influence of etching conditions on apatite fission-track etch pit diameter. Chem. Geol. 271(1-2), 59-69.

Stockli, D.F., Linn, J.K., Walker, J.D., Dumitru, T.A., 2001. Miocene unroofing of the Canyon Range during extension along the Sevier Desert Detachment, west central Utah. Tectonics 20, 289-307.

Stormer Jr., J.C., Milton, L.P., Tacker, R.C., 1993. Variation of F and Cl X-ray intensity due to anisotropic diffusion in apatite during electron microprobe analysis. Am. Mineralog. 78, 641-648.

Sudarsanan, K., Young, R.A., 1978. Structural interactions of F, Cl and OH in apatite. Acta Crystallogr. B34, 1401-1407.

Van den haute, P., De Corte, F. (eds), 1998. Advances in Fission-Track Geochronology. Kulwer Academic Publishers, Dordrecht.

Villa, F., Grivet, M., Rebetez, M., Dubois, C., Chambaudet, A., 1997. Calibration and simulation of apatite fission track etching: Influence of diffusion and crystal symmetry. Radiat. Meas. 28(1-6), 543-548.

Villa, F., Grivet, M., Rebetez, M. Dubois, C., Chambaudet, A., Chevarier, N., Blondiaux, G., Saugave, T., Toulemonde, M., 2000. Damage morphology of Kr ion tracks in apatite: Dependence on thermal annealing. Nucl. Inst. Meth. Phys. Res. B 168, 72-77.

Villa, F., Grivet, M., Rebetez, M., Dubois, C., Chambaudet, A., Chevarier, A., Martin, P., Brossard, F., Blondiaux, G., Sauvage, T., Toulemonde, M., 1999. Damage morphology of Kr ion tracks in apatite: Dependence on dE/dX. Radiat. Meas. 31, 65-70.

Vrolijk, P., Donelick, R.A., Queng, J., Cloos, M., 1992. 7. Testing models of fission track annealing in apatite in a simple thermal setting: Site 800, leg 129. Proc. Ocean Drill. Prog., Sci. Results 129, 169-176.

Wagner, G.A., 1969. Spuren der spontanen Kernspaltung des [238]Urans als Mittel zur Datierung von Apatiten und ein Beitrag zur Geochronologie des Odenwaldes. N. Jahrb. Mineralog. Abh. 110, 252-286.

Wagner, G.A., Storzer, D., 1972. Fission track length reductions in minerals and the thermal history of rocks. Trans. Am. Nucl. Soc. 15, 127-128.

Wagner, G.A., Van den haute, P., 1992. Fission Track Dating. Kulwer Academic Publishers, Dordrecht.

Wendt, A.S., Vidal, O., Chadderton, L.T., 2002. Experimental evidence for the pressure dependence of fission track annealing in apatite. Earth Planet. Sci. Lett. 201, 593-607.

Young, E.J., Myers, A.T., Munson, E.L., Conklin, N.M., 1969. Mineralogy and geochemistry of fluorapatite from Cerro de Mercado, Durango, Mexico. Geol. Surv. Prof. Paper 650D, D84.

Zhang, J.M., Lang, M., Lian, J., Liu, J., Trautmann, C., Della-Negra, S., Toulemonde, M., Ewing, R.C., 2009. Liquid-like phase formation in $Gd_2Zr_2O_7$ by extremely ionizing irradiation. J. Appl. Phys. 105, 113510.

Ziegler, J.F., Ziegler, M.D., Biersack, J.P., 2010. SRIM - The stopping and range of ions in matter. Nucl. Inst. Meth. Phys. Res. B 268 (11-12), 1818-1823.

## 8. Appendix: Anomalous etching behaviors revealed by etch pit morphology

As mentioned in Section 4.2, it appears that track etching may have more complex controls than damage production and annealing kinetics. In fact, simple observation of etch pit morphology indicates track etching behavior is inherently complex and even contradictory. For example, why should Otter Lake etch figures be larger than Durango etch figures for all orientations except one? Why should Otter Lake etch figures be asymmetrical, given that this behavior violates basic principles of crystal symmetry?

While these questions are made obvious by simple examination of Figure 13, other contradictions displayed by etch tracks require more explanation. For example, since Durango (0001) etch figures are wider than etch figures of other orientations (Fig. 13), it would seem logical to conclude that, in general, track etch rates in apatite are highest in the directions perpendicular to the *c*-axis. However, Durango etch figures on the *c*-axis parallel orientations – (10-10) and (2-1-10) – show elongation *parallel* to the *c*-axis, suggesting that etch rates are faster in the *c*-axis direction than perpendicular to it. This orientation dependence is related to the atomic structure in the direction parallel to the track length. In the case of (0001) tracks, tracks are oriented down the hexagonal channels. These channels may allow more efficient etching of (0001) tracks, resulting in higher *c*-axis-perpendicular etch rates measured for (0001) tracks than for (10-10) or (2-1-10) tracks.

While the different etch rates between *c*-axis parallel and *c*-axis perpendicular tracks can be explained by the hexagonal channels, there is also a discrepancy between *c*-axis perpendicular tracks themselves. Otter Lake (2-1-10) etch figures have larger diameters than Otter Lake (2-1-10) etch figures, even though both are from tracks running parallel to the *c*-axis, and in both cases diameters are measured in the same direction – parallel to the *c*-axis. Thus track etch rates are dependent not only upon the orientation of the track with respect to the *c*-axis, but also upon the track orientation with respect to the *a*-axes (Figs. 1, 12). As discussed in the Results, etch figure *width* is clearly higher for Otter Lake (10-10) than for Otter Lake (2-1-10) (Fig. 13). This is understandable when compared with (0001) etch figures, which show greater width in the (10-10) direction than in the (2-1-10) direction (see Figure A1). While it may be logical to expect that greater width results in greater length due to enhanced etchant diffusion into the track, this is not the case. Thus the greater etch figure diameters for the Otter Lake (2-1-10) samples relative to Otter Lake (10-10) samples is inexplicable. Further complicating this analysis is the reversal of relative sizes between Otter Lake (10-10) and (2-1-10) etch figures upon annealing, due to the greater observed etch figure diameter reduction of the latter as a function of increasing temperature. Thus annealing may show a dependence on track orientation relative to the *a*-axis as well.

A final anomalous etching behavior discussed in the Results section is that weaker etchant concentrations show more isotropic etching than stronger etchants, resulting in lower etch figure aspect ratios for lower etchant concentrations (Fig. 14). Although reported in Ravenhurst et al. (2003), there is no explanation therein. It is obvious that stronger etchants remove amorphous material more quickly, and thus varying etching in the track-parallel direction likely plays a role in determining

etch rates in the track-perpendicular dimension. This phenomenon may be related to the diffusion limitations of etching discussed by Villa et al. (1997).
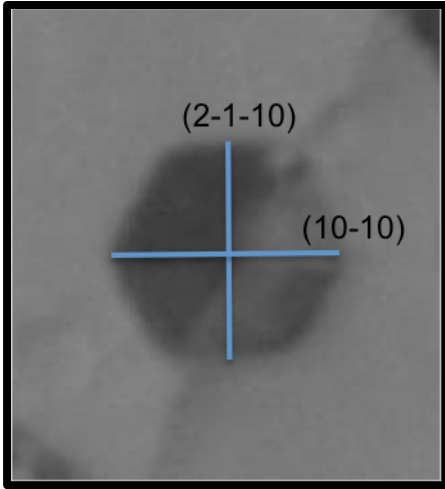
Figure A1: A typical apatite (0001) etch figure, showing greater width in along the (10-10) orientation than along the (2-1-10) orientation.